Acoustics Australia
https://doi.org/10.1007/s40857-025-00352-4

ORIGINAL PAPER

Reducing Tonal Noise of Contra-Rotating Unmanned Aerial System Rotors via Blade Rake Angle Adjustment

Riul Jung[1] · Carlos Ramos-Romero[1] · Michael J. Kingan[2] · Deepak Akiwate[1] · Antonio J. Torija[1]

Received: 23 January 2025 / Accepted: 5 May 2025

Abstract
This paper investigates the effect of blade rake angle on the tonal noise produced by contra-rotating rotor systems suitable for use on small multi-rotor unmanned aerial systems (UAS). This investigation utilises semi-analytical, numerical, and experimental methods to investigate the physics of the noise generation mechanisms, generated noise levels and the psychoacoustic characteristics of this noise. Computational fluid dynamics (CFD) simulations and semi-analytical models are employed to predict the periodic unsteady loading on the rotor blades, and the loading data are used to predict the radiated noise for rotor systems with different blade rake angles. Experimental measurements of the noise produced by a rotor system with no blade rake angle were used as a baseline case, and predictions were used to synthesise and auralise the sound produced by rotor systems with different rake angles for psychoacoustic analysis. The results show that increasing the blade rake angle generally reduces the amplitude of prominent interaction tones due to the reduction in the unsteady loading along the blade span caused by bound potential field interactions as the blade rake angle increases. This causes a reduction in the perceived tonal noise level.

Keywords Aeroacoustics · Psychoacoustics · Contra-rotating UAS rotor · UAS propeller noise

1 Introduction

Unmanned aerial systems (UASs) are a growing technology for a wide range of applications, from parcel delivery to survey and search and rescue. A multi-rotor UAS typically utilises 4, 6 or 8 single rotors to provide the thrust required for flight. However, contra-rotating rotor systems, such as that shown in Fig. 1, can be used instead, and they offer several advantages over single-rotor systems. For example, they generate less torque on the airframe [1]; the lower rotor can mitigate the wake swirl from the upper rotor, enhancing the aerodynamic efficiency [2]; and the additional rotor provides redundancy in case of failure. However, a notable drawback of contra-rotating rotor systems is the significant levels of tonal noise which they produce compared with equivalent single-rotor systems [1].

This tonal noise is due to the periodic unsteady loading on the rotor blades caused by their interaction with the unsteady aerodynamic field produced by the adjacent rotor. This unsteady aerodynamic field can be thought of as consisting of a sum of flow disturbances—namely the viscous wakes shed from the trailing edges of the rotor blades, the tip vortices and the bound potential field [3]. The bound potential field is the flow disturbance caused by the loading on, and thickness of, the rotor blades.

There have been several recent studies on the noise produced by contra-rotating UAV rotor systems. For example, McKay et al. [1, 4] explored the effect of rotor–rotor spacing, rotor diameter, rotor speed and number of blades on the noise which was produced. Their results and analysis demonstrated

✉ Riul Jung
R.jung@salford.ac.uk

Carlos Ramos-Romero
C.A.RamosRomero@salford.ac.uk

Michael J. Kingan
M.kingan@auckland.ac.nz

Deepak Akiwate
D.C.Akiwate@salford.ac.uk

Antonio J. Torija
A.J.ToriaMartinez@salford.ac.uk

[1] Acoustics Research Centre, University of Salford, Manchester, UK

[2] Acoustics Research Centre, Department of Mechanical and Mechatronics Engineering, The University of Auckland, Auckland, New Zealand

Published online: 31 May 2025

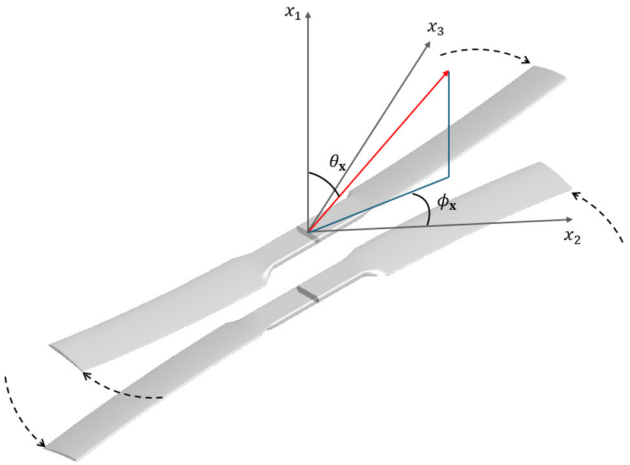

Fig. 1 Schematic of a contra-rotating rotor system showing the direction of rotation of both rotors and the spherical coordinate system used to specify the observer's location utilised in this paper

a number of important findings: in particular, they showed that rotor systems with different numbers of blades on the top and bottom rotors produced significantly lower levels of tonal noise at observer positions close to the rotor axis; they also observed that as the rotor–rotor spacing increased, the interaction tone noise levels decreased significantly which they suggested was likely due to the reduction in the strength of the bound potential field incident on each rotor. A number of subsequent studies [5–7] have confirmed that the dominant noise generation mechanism for configurations with small rotor–rotor spacings is the unsteady loading produced by the bound potential field interactions. At larger rotor–rotor spacings, the tip vortex from the upper rotor interacting with the lower rotor (and generating unsteady loading on the outer portion of the lower rotor) is a dominant noise source [5]. More recently, Jung et al. [8] studied the effect of blade skew on the interaction tones produced by a contra-rotating UAV rotor system. They demonstrated that significant noise reductions can be achieved by skewing the blades in order to offset the rotor–rotor interactions along the blade span.

In addition to studies solely investigating the physics of the noise generation mechanisms and methods for reducing them, there have been a number of studies exploring the perception of contra-rotating UAS noise and how changes in rotor system geometry and operating conditions affect this. For example, Torija et al. [9] used experimental measurements to assess how varying the rotor–rotor spacing affected various psychoacoustic metrics and thus how annoyance caused by this noise can be minimised. Similarly, Hirono et al. [10] used experimental data to assess the effect of rotor blade number and rotor–rotor spacing on various noise metrics at different observer locations. The noise metrics used in the study included loudness, fluctuation strength, roughness, tonality, and impulsiveness. They identified rotor blade count numbers and rotor–rotor spacings which produced noise which was lower in level and less annoying than other measured configurations.

This paper describes an investigation of the effect of blade rake angle on the interaction tones generated by contra-rotating UAS rotor blades, using semi-analytical, numerical, experimental, and psychoacoustic methods. The rotor system geometry and operating conditions considered in this paper are defined in Sect. 2.1. Section 2.2 briefly describes the numerical simulation methods and semi-analytical models used to calculate the unsteady loading on the rotor blades and also describes the method used to calculate the radiated sound pressure. The experimental methods used to measure the noise produced by the baseline contra-rotating rotor system are described in Sect. 2.3, and the psychoacoustics analysis method is summarised in Sect. 2.4. Section 3 includes an analysis of the predicted blade loading (Sect. 3.1) and a comparison of the predicted and measured noise levels and analysis of the effect of blade rake angle on the predicted noise levels (Sect. 3.2–3.3). The effect of blade rake angle on the psychoacoustic tonality is explored, and the results are presented in Sect. 3.4.

2 Methodology

2.1 Rotor Geometry and Operating Conditions

The rotor blades used in this study all have a constant section profile along the radius of the blade. The profile has a chord length of 26.6 mm, a maximum thickness of 7.33% of the chord length, and a pitch angle of 8°. The profile is also cambered with maximum camber of 3.76% of the chord length which is located at 55% of the chord length from the leading edge. All blades considered in this paper have a tip radius of 190.5 mm and a hub radius of 35 mm. The rotor blades are either straight or curved which is defined by the blade tip rake angle, $\theta_{\mathbf{rake}}$. The definition of the blade tip rake angle is shown in Fig. 2. For the blades considered in this paper, the blade mid-chord lies at the same azimuthal angle but is located at a polar angle, θ (measured from the centre of the rotor being considered), given by:

$$(r) = \theta_0 \pm \theta_{\mathbf{rake}} \frac{(r - r_h)}{(r_t - r_h)},\ r_h \leq r \leq r_t, \tag{1}$$

where $\theta(r)$ is the polar angle of the blade mid-chord at radius r. $\theta_{\mathbf{rake}}$ is the change in polar angle of the blade mid-chord between the hub radius, r_h and the tip radius of the blade, r_t. θ_0 is equal to 90°, and $\pm$ sign indicates the direction of the rake adjustment, depending on whether the blade is on the top (−) or bottom (+) rotor.

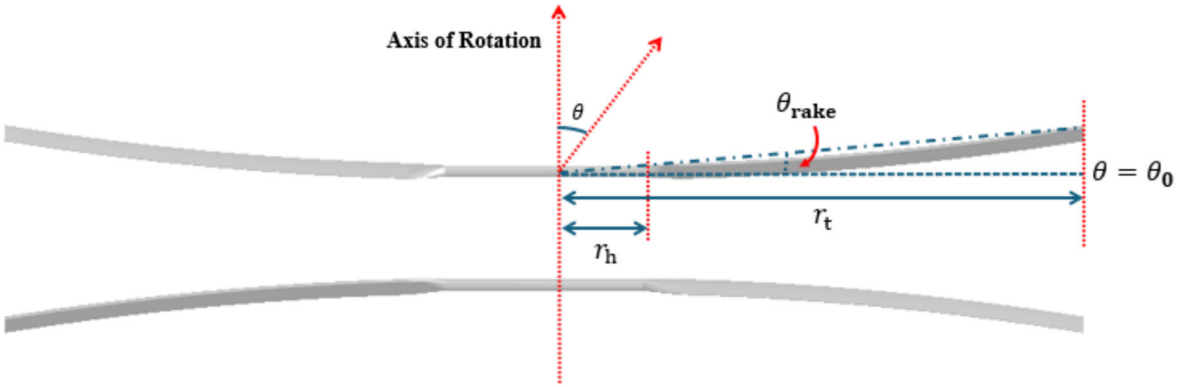

Fig. 2 Illustration of the contra-rotating UAS rotor showing the definition of the tip blade rake angle for the top rotor

In this study, two different contra-rotating rotor systems were analysed. In the first system, both the top and bottom rotor blades had a blade tip rake angle of $\theta_{\mathbf{rake}} = 0°$ (i.e. the blades were straight), whilst the second system had blades with a tip rake angle of $\theta_{\mathbf{rake}} = 10°$. In the second system, the rake angle increases the separation distance between the top and bottom blades along the blade span. The axial separation distance at the hub for both systems was 40 mm. For all systems considered in this study, both top and bottom rotors rotated at 500 rad/s with the top rotor rotating clockwise and the bottom rotor rotating counterclockwise when viewed from above.

2.2 Aerodynamic Loading and Noise Radiation Calculation Methods

In this section, the methods used to calculate the aerodynamic loading and radiated acoustic pressure are described. The aerodynamic loading was calculated using both computational fluid dynamics (CFD) simulations and semi-analytical models and the data was used as an input to the frequency-domain method used to calculate the radiated acoustic pressure. The CFD-based method was the primary prediction tool, whilst the semi-analytical model acted as a secondary tool to identify the main causes of unsteady blade loading and to provide insights into the noise generation mechanisms.

CFD simulations were conducted to calculate the periodic unsteady loading on the blades of the rotors, using a method similar to that presented in Jung et al. [7, 8]. The simulations did not include the geometry of the electric motors and shafts which drove the rotors. This was justified because these features have little effect on the flow through the rotor system—in particular on the periodic loading on the outer sections of the blades (which is the primarily cause of the interaction tones produced by the rotor system). The simulations utilised the overset mesh method [11] where the complex geometry of the rotor blades was meshed using a hexacore mesh as shown in Fig. 3. A separate component mesh surrounded each rotor and was refined so that the y^+ values of the closest mesh nodes to the blade surfaces was less than one. The component meshes were superimposed onto cylinder-shaped background meshes (with a diameter slightly larger than that of the rotors) which rotated with the component meshes at the speed of the rotors. The rotating domains surrounding each rotor comprised a component mesh and a background mesh. The top and bottom rotating domains were separated by a sliding mesh interface. The two rotating domains were surrounded by a cylinder-shaped static domain. The top and side surfaces of the static domain were set as pressure-inlets, and the bottom surface was set as a pressure outlet as shown in Fig. 3. The static domain had a diameter and height equal to two and three times the diameter of the rotors, respectively.

The simulations were conducted using ANSYS Fluent [11] and solved the incompressible, unsteady Reynolds-averaged Navier–Stokes (URANS) equations using the $k-\omega$ shear stress transport turbulence model with transition model. The pressure-based solver was used with the semi-implicit method for pressure-linked equations (SIMPLE) algorithm. The transient simulations were initialised using the solution obtained from a steady RANS calculation, which was obtained using Fluent's multiple reference frame (MRF) model. For the transient simulations, the time-step size was chosen such that both top and bottom rotors rotated at 1° per time step. For all the simulations presented in this paper, the number of iterations per time step was chosen so that the normalised residuals reduced to a value less than 10^{-5} before the simulations moved to the next step. The transient simulations were run for three revolutions, which was sufficient to observe periodic behaviour in the total forces acting on both rotors. As the transient simulations only completed three full revolutions of the rotors, the wake well downstream of the rotors may not be fully developed. This was judged not to be a significant effect for the simulations as the total thrust acting on each rotor became periodic before the completion of the third full rotation of the rotors, indicating that the

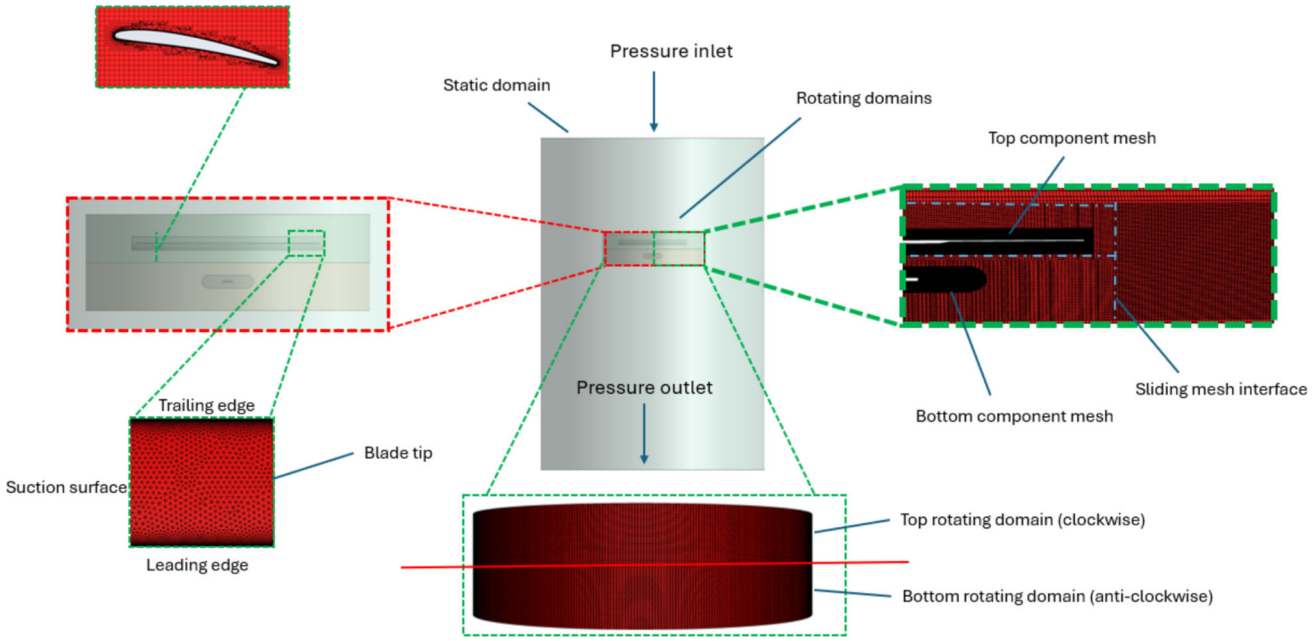

Fig. 3 Illustration of the mesh interlink between the static and rotating domains with the connectivity between the background and component mesh. The boundary conditions are also displayed

Table 1 Grid independence study for blades with $\boldsymbol{\theta}_{\mathbf{rake}} = 0°$

	Coarse	Medium	Fine
Number of cells	6,554,353	12,957,415	18,121,031
Averaged total thrust (N)	17.5810	18.6481	18.6420

Table 2 Grid independence study for blades with $\boldsymbol{\theta}_{\mathbf{rake}} = 10°$

	Coarse	Medium	Fine
Number of cells	11,082,798	13,419,532	16,146,709
Averaged total thrust (N)	17.7621	17.7886	17.833

flow features influencing the blade loading did not change with each blade-to-blade interaction. The estimated time-averaged thrust level produced by the baseline case where the rake angle of the blades, is zero was 18.64 N which compares with 17.79 N for the case where the rake angle was 10°. The measured thrust level for the baseline case was 17.4 N, with a percentage difference of 6.1% between the measured and predicted values.

Grid independence studies were undertaken for the simulations of both systems. These studies showed that the total unsteady loading acting on the rotor systems was approximately independent of the number of mesh cells. The mesh used to analyse the rotor system with blade tip rake angle $\theta_{\mathbf{rake}} = 0°$ had 18.12×10^6 cells, and the rotor system with blade tip rake angle $\theta_{\mathbf{rake}} = 10°$ had 13.42×10^6 cells. The results of the grid independence study are shown in Tables 1 and 2. The simulations were conducted using a Cray XC50 supercomputer using 36 CPU cores. The steady RANS simulations for both systems took approximately 6 h whilst the transient solutions required between 30 and 42 h to simulate three revolutions of the rotors.

The semi-analytical model described in Jung et al. [7] was also used to calculate the blade loading for both rotor systems with blade tip rake angles of $\theta_{\mathbf{rake}} = 0°$ and 10°. Note that these methods were also used by Jung et al. [8] to study the effect of blade skew on the interaction tones produced by the contra-rotating rotor system. This method models the unsteady loading caused by the bound potential field interactions and is used to demonstrate the effect of blade rake angle on these interactions and the resulting unsteady loading. Whilst CFD simulations are computationally very expensive, the semi-analytical models can be used as a rapid prediction tool which will be invaluable for parametric studies in the early design stage. The CFD simulations conducted in this work for calculating the loading data took up to 48 h on a Cray XC50 supercomputer using 36 CPU cores, whereas the predictions of the unsteady blade loading using the semi-analytical model typically took approximately 30 s using a standard laptop (Intel Core i7-12700H CPU @ 2.30 GHz, 32 GB RAM).

The semi-analytical modelling process is as follows. Firstly, the geometry and rotational speeds of the top and bottom rotors are specified. The relevant geometric parameters

for each rotor include the number of blades, tip radius, chord length and thickness distribution and the axial and tangential locations of the mid-chord along the blade radius. The next step is to estimate the steady loading acting on the top and bottom propellers and estimate the axial induced velocity of the flow through the rotors. In the work reported in this paper, these estimates were made using data from the CFD simulations (although these quantities could also be estimated using low-fidelity methods such as the blade element and momentum method). From these estimates, the amplitude of the Fourier harmonic of the velocity perturbation incident on the reference blade of a rotor due to the bound potential field produced by the loading and thickness sources on the blades adjacent rotor are calculated using eqs A15, A19 and A28 and A31, respectively, from Ref. [7]. The corresponding unsteady loading produced by each incident velocity harmonic is then calculated using eqs A16, A18, A29 and A30, respectively, from Ref. [7]. The unsteady loading harmonics can then be summed together to give a total unsteady loading time-history, or the harmonics directly used in a frequency-domain noise prediction method such as that described in Ref. [7].

The radiated acoustic pressure was calculated using the frequency-domain method also described by Jung et al. [7] which is similar to that presented by Hanson [3], but which allows a more accurate representation of the acoustic sources on the rotor blades. This method requires the blade loading to be decomposed into a temporal Fourier series. The amplitude of the Fourier harmonics is then input into the noise prediction method which directly predicts the amplitudes of the interaction tones of interest. High-fidelity noise predictions were made using the unsteady loading data on the surfaces of the rotor blades calculated from the CFD simulations. These data for the rotor were decomposed into Fourier harmonics which were used as inputs into Eqs. 18–20 in Ref. [7]. These equations were used along with Eq. 21 for the bottom and Eq. 24 for the top rotor. For predictions made using the unsteady loading from the semi-analytical models, simpler expressions incorporating Eqs. (22) and (25) in Ref. [7] are used instead. These simplified expressions assume that the radial loading can be neglected and that the blade chord is sufficiently small such that the blades are acoustically compact in the chordwise direction. The method has been validated by comparing its implementation with predictions calculated using Farassat's formulation 1A [12, 13] which is a commonly used time-domain method. The frequency-domain method is preferable to time-domain methods when using CFD data as it only requires one period of loading data, whereas the time-domain method requires several revolutions of loading data (the exact number depends on the blade numbers and rotational speeds) which can be computationally expensive.

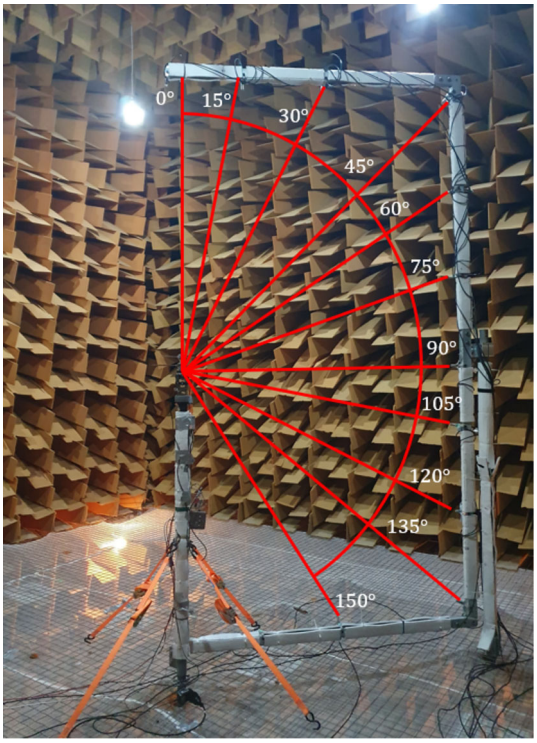

Fig. 4 Photograph of the contra-rotating UAS rotor system mounted in the anechoic chamber at the University of Auckland. The C-shaped microphone array with absorbing foam is shown along with the polar angle of the microphones

2.3 Experimental Methods

Acoustic measurements were conducted to measure the radiated acoustic pressure from the baseline case (i.e. the system with rotors with straight blades) in the anechoic chamber at the University of Auckland. The anechoic chamber at the University of Auckland has internal dimensions of 5.3 m × 5.3 m × 5.3 m and has a cut-off frequency below 80 Hz. The experimental setup is shown in Fig. 4. The contra-rotating rotor system was mounted on a Honeywell model 151 S-type load cell which was used to measure thrust. This in turn was mounted on a vertical pole in the centre of the anechoic chamber. The rotors were driven by a custom-made contra-rotating motor unit which consisted of two T-Motor MN501 motors. The motors were controlled using two T-Motor alpha electronic speed controllers powered by a 48V power supply. Acoustic measurements were made using 11 G.R.A.S 46AE 1/2″ microphones covering polar angles, $\theta_{\mathbf{x}}$, between 0° and 150° in increments of 15°. The polar angle for the acoustic measurements was measured from the centre of the top rotor. Measurements at polar angles of 165° or larger were not made because prior experience showed that the noise signals measured at these locations could be contaminated by airflow from the rotor system. The data acquisition system comprised NI9234 modules mounted in an NI cDAQ and the

data was acquired over 30 s at a sampling rate of 51.2 kHz for each measurement. This experiment used the same test rig to that used by Jung et al. [7, 8]. The microphones were mounted on a C-shaped support structure, and this structure and the pole onto which the rotor system was mounted were lagged in sound absorbing foam to minimise the effect of reflections from these surfaces. Note that all acoustic measurements were normalised to a spherical radius of 1.5 m assuming spherical spreading from the centre of the top rotor.

2.4 Auralisation and Psychoacoustic Methods

Only acoustic measurements of the rotor system with blade tip rake angle $\theta_{\mathbf{rake}} = 0°$ (i.e. straight blades) were available. To enable the psychoacoustic analysis of the other rotor system with the raked blades, a recording-based method for synthesis and auralisation was applied, following procedures described in Ramos-Romero et al. [14]. This step is particularly important, because even if the noise levels due to the raked blade design has been reduced, the human perception of the altered noise level needs to be evaluated to fully understand the implications of the noise reduction.

The general calculation procedure to predict sound quality metrics for a rotor system with different blade rake angle is shown in Fig. 5. Firstly, the noise measurements of the baseline rotor system were obtained from tests conducted in the anechoic chamber at the University of Auckland. Then synthesis methods were applied to separate out the tonal noise from the broadband components of the signal. The method for synthesis and auralisation applied in this work involved using a cascaded second order sections filter bank to process the recorded signal. This method tracks the spectral features of the broadband component of the propeller noise. These filters were then applied to white noise, creating the synthesised broadband noise component. This process enables accurate reproduction and analysis of the broadband characteristics of the original noise recording. The tonal noise component was generated using the additive synthesis method, which involved modelling the tonal noise as a linear combination of sinusoidal signals (see Romero et al. [14] for further details). To validate the synthesised noise signal, the combined estimated broadband noise and tonal noise were compared with the original recording of the rotor system with straight blades. Comparisons of the spectrograms of Tonal Loudness and Tonality calculated for the original recording and the synthesised audio data confirmed that the synthesised signal was suitable for assessing the psychoacoustic effect of the noise produced by the UAV rotors. The comparison of these plots is presented in Fig. 23 and 24 in the Appendix.

The sound pressure levels of tones at the blade passing frequency and its harmonics were calculated for both rotor systems using the prediction methods outlined in Sect. 2.2 (using CFD loading data). The amplitude changes due to the increase in the blade tip rake angle calculated from these simulations were applied to the separated tonal noise components from the measurements of the baseline case. The adjusted tonal sound pressure levels were then combined with the baseline broadband noise to synthesise the expected noise for the rotor system with a blade tip rake angle of $\theta_{\mathbf{rake}} = 10°$. The broadband level was assumed to remain constant for both rotor systems, so no modifications to the broadband noise levels were made. This assumption is justified as it is expected that the dominant broadband noise generation mechanism is rotor self-noise which, provided the rotor aerodynamics are similar for both cases, the broadband noise levels should also remain similar. A similar phenomenon was observed by Deepak et al. [15] for single rotors.

The Sound Quality Metrics (SQMs) Tonal Loudness and Tonality were used to estimate the psychoacoustic effect of changing the blade tip rake angle. These metrics were calculated using the ArtemiS Suite software [16] which implements Sottek's Hearing Model [17]. The Tonality metric describes how spectral irregularities or discrete tones are perceived [18], and the Tonal Loudness metric accounts for the prominence of all tonal noise over broadband noise in a sound signal. In this paper, the SQMs were calculated from the synthesised signal for the baseline case (i.e. blade tip rake angle of $\theta_{\mathbf{rake}} = 0°$) and the estimated noise signal for the rotor system with a blade tip rake angle of $\theta_{\mathbf{rake}} = 10°$.

To summarise the test cases investigated in this work, Table 3 has been presented. It includes operating conditions, Reynolds number and what cases were investigated using CFD simulations, semi-analytical models and experiments.

3 Results and Discussion

3.1 Unsteady Loading Analysis

The noise produced by a contra-rotating UAS rotor is dominated by the interaction tones produced by the periodic unsteady loading on the rotor blades. It is therefore useful to analyse this unsteady loading. For this purpose, the reference blade of each rotor was divided into 10 radial segments and the unsteady force acting on each segment was calculated using the data from the CFD simulations and semi-analytical models for both rotor systems (with straight blades and raked blades) considered in this paper. Whilst the CFD simulations include all important features of the flow field through the rotor systems, the semi-analytical models only include the effects of the bound potential field interactions. The comparison of the unsteady loading calculated using both methods allows us to explore the primary causes of the impulses in the unsteady loading.

In Figs. 6 and 7, contour plots of the calculated unsteady axial force per unit span acting on each segment of the top

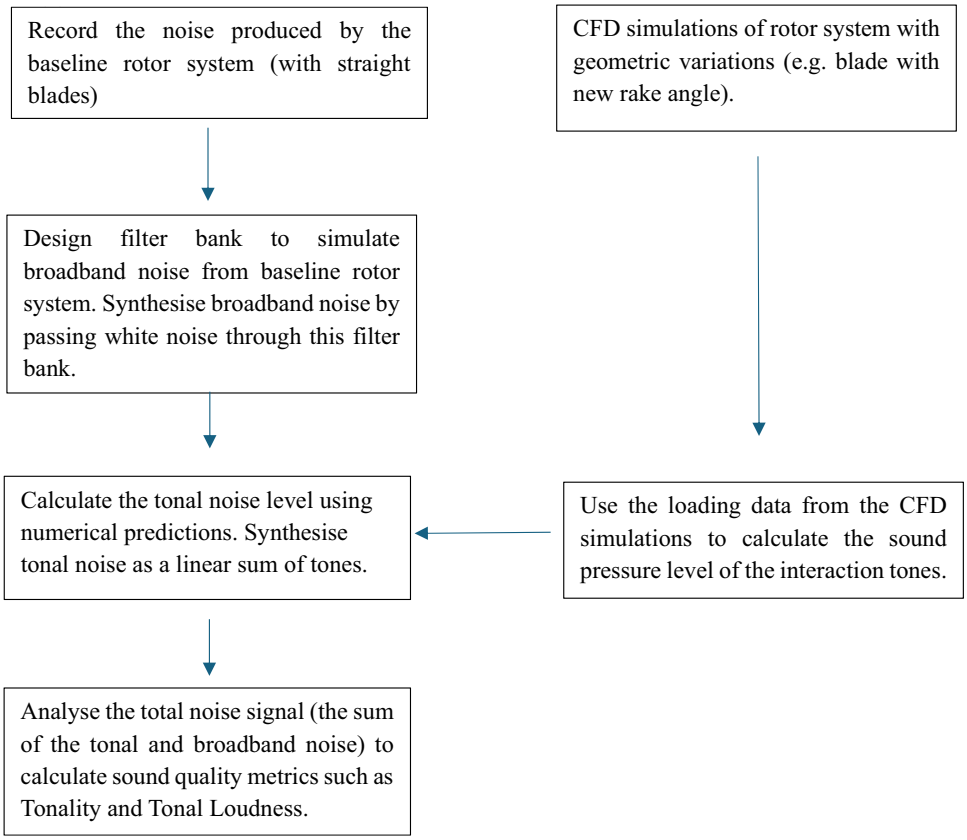

Fig. 5 Schematic showing the procedure for calculating the sound quality metrics for rotor systems via noise synthesis methods

Table 3 Summary of the test cases investigated in this work

	Blade rake angle	Rotational speed (top and bottom)	Reynolds number at the tip	CFD investigation?	Semi-analytical method	Experiments	Synthesised signal?
Case 1	0°	500 rad/s	170,832	Yes	Yes	Yes	Yes
Case 2	10°	500 rad/s	170,832	Yes	Yes	No	Yes

and bottom rotor reference blades are plotted against non-dimensional radius (vertical axis) and non-dimensional time (horizontal axis) for rotor systems with straight and raked blades. In these contour plots, the y-axis is normalised by the tip radius, r_t, and the x-axis is normalised by the blade–blade interaction period of the top rotor (which is identical to that of the bottom rotor due to the fact that both rotors have two blades), $T = 2\pi/(\Omega_1 + \Omega_2)/B_2$, where Ω_1 and Ω_2 are the rotational speeds of the top and bottom rotors, respectively, and B_2 is number of blades on the bottom rotor. Each figure comprises four subplots. The two left-hand side subplots in Figs. 6 and 7 present the results calculated from the CFD simulations, and the two subplots on the right-hand side present the results calculated using the semi-analytical models. The two top subplots in Figs. 6 and 7 show the results for the rotor system with straight blades, whilst the bottom two subplots show the results for the rotor system with the raked blades. In these results, the times at which the mid-chords of the top and bottom rotor blades pass over each other are shown with red dashed lines on each plot. For all plots, the impulsive loading produced due to the bound potential field interactions occurs close to these times. Additionally, for the results calculated using CFD simulation data for the bottom rotor reference blades, red ovals are plotted at times where the tip vortex produced by the top rotor blades was estimated to impinge on the bottom reference blade.

Figure 6 presents the results for the top rotor reference blades of both rotor systems. There is good agreement between the CFD simulation results, and the results calculated using the semi-analytical model. The semi-analytical model predicts maximum and minimum forces, which are, on average, within 17% of those predicted by the CFD method for the outer 10% portions of the straight and raked top rotor blades. This is expected as the only source of periodic

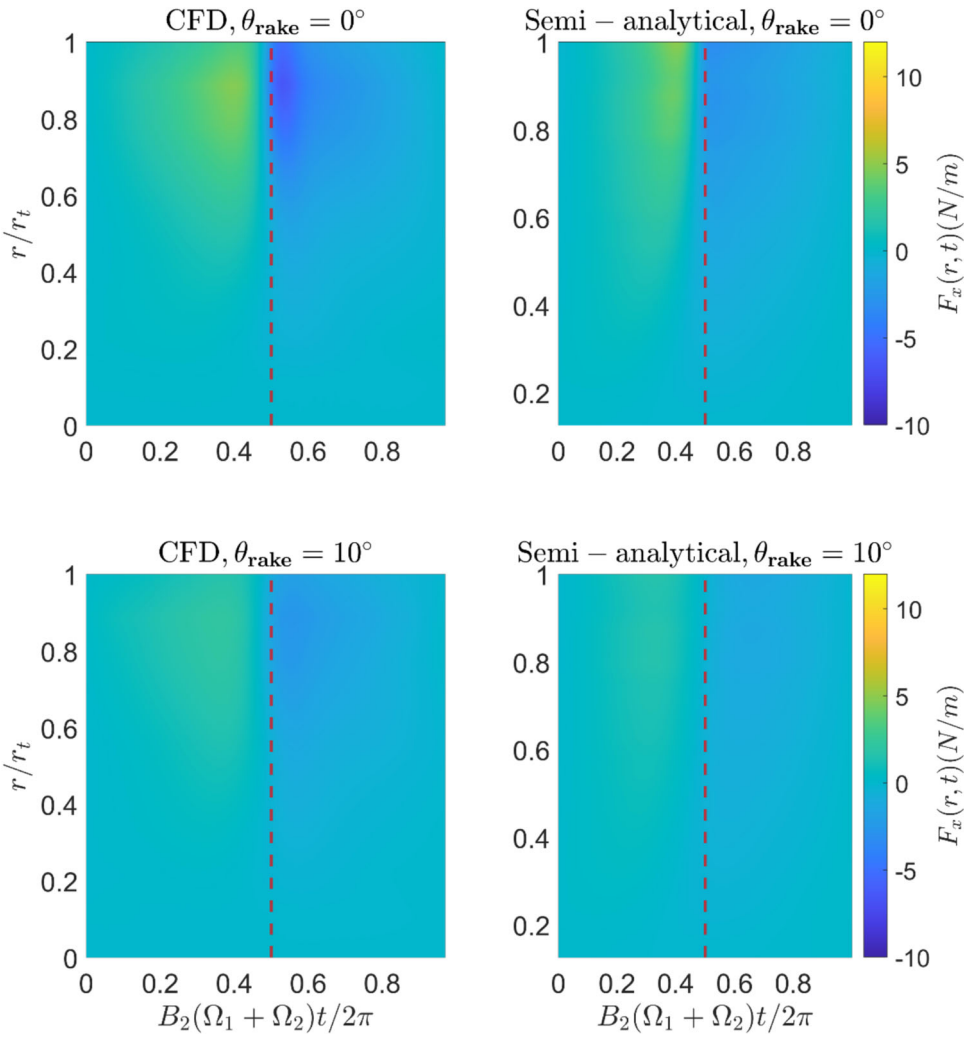

Fig. 6 Contour plots of the unsteady axial force per unit span calculated from the CFD simulations (left) and semi-analytical model (right) for the top rotor reference blade plotted against dimensionless radius (vertical axis) and dimensionless time (horizontal axis). Results for the rotor system with straight blades are shown in the top subplots, whilst the results for the rotor system with raked blades are shown in the bottom subplots. The dashed red lines show the times at which the mid-chords of the top and bottom rotor reference blades pass over each other

unsteady loading on the top rotor blades is the bound potential field produced by the bottom rotor and this effect is captured by both prediction methods. It is observed that the magnitude of the unsteady loading produced close to the times where the top and bottom rotor blades pass over each other is lower for the raked blades in comparison to the straight blades. This is because the rake angle of the blade increases the axial distance between the top and bottom rotor blades along the blade span which, in turn, reduces the strength of the bound potential field and the magnitude of the associated impulsive loading. The difference in the magnitude of the unsteady loading between the straight and raked blades is particularly large on the outer portions of the blades where the axial separation of the raked blades is largest. A similar effect was observed by McKay et al. [1], where it was shown that as the axial distance between two contra-rotating UAV rotors with straight blades increased, the magnitude of the estimated unsteady loading decreased (which was attributed to the reduction in the bound potential field effect).

Figure 7 presents the corresponding results calculated for the bottom rotor reference blades. As expected, there are differences between the results from the CFD simulations and the semi-analytical models. This is because the CFD simulations include the effect of the tip vortices which are shed from the blade tips of the top rotor and interact with the bottom rotor blades, whereas the semi-analytical model only accounts for the bound potential field interactions. This tip vortex interaction produces unsteady loading on the outer potion of the blade. The times at which the tip vortex interacts with the bottom rotor reference blade was estimated by visualising the tip vortex using iso-surfaces of constant lambda-2 criterion and identifying where the iso-surfaces interacted with the bottom reference blade. For both systems, the impingement of the tip vortices occurs at radii between 83 and 92% of the blade tip radius (note that the tip vortices migrate radially inwards as they convect downstream due to the stream tube contraction downstream of the top rotor). However, the times at which the tip vortex interacts with the bottom reference blade are different for both rotor

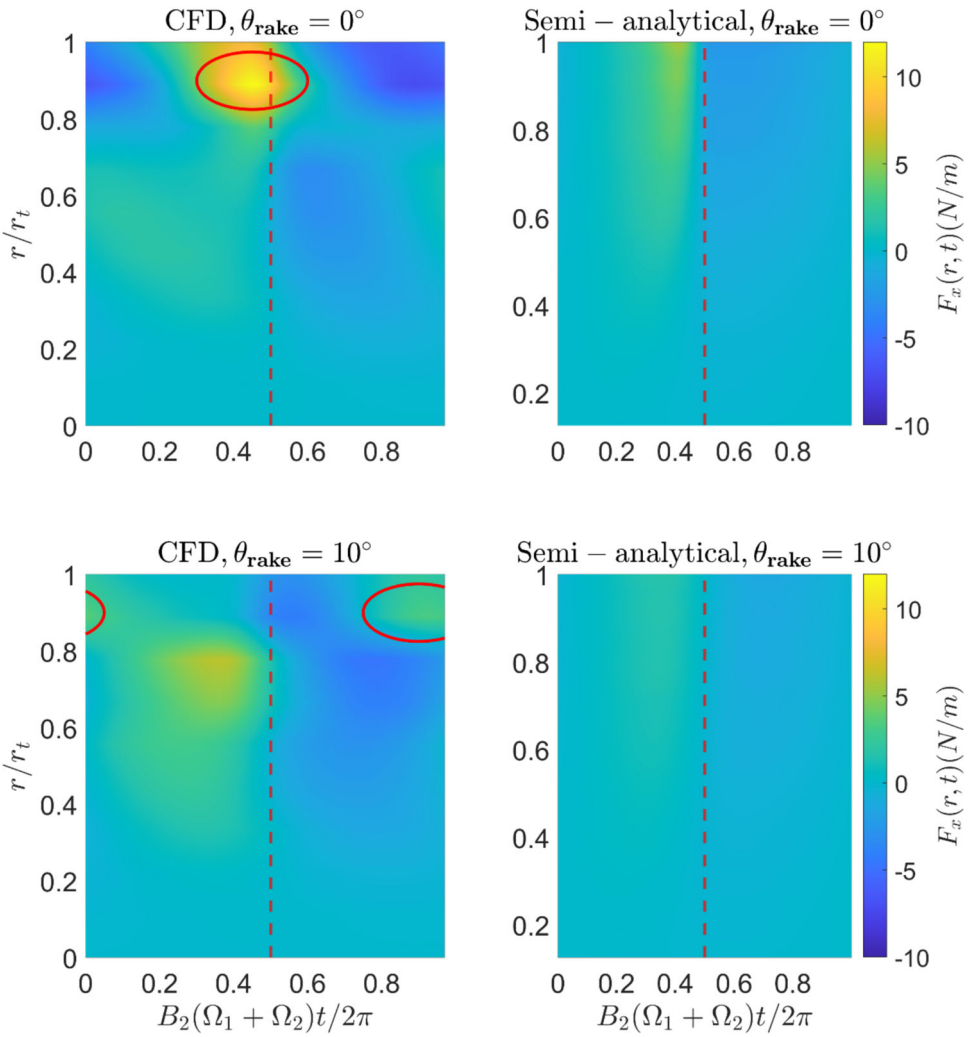

Fig. 7 Contour plots of the unsteady axial force per unit span calculated from the CFD simulations (left) and semi-analytical model (right) for the bottom rotor reference blade plotted against dimensionless radius (vertical axis) and dimensionless time (horizontal axis). Results for the rotor system with straight blades are shown in the top subplots, whilst the results for the rotor system with raked blades are shown in the bottom subplots. The dashed red lines show the times at which the mid-chords of the top and bottom rotor reference blades pass over each other. The red ovals indicate the times and radial locations at which the tip vortex interacts with the bottom reference blade

systems. For the rotor system with the straight blades, the tip vortex interaction occurs close to the times when the mid-chords of the top and bottom blades pass each other which is also close to the times at which the potential field interactions occur. For the rotor system with the raked blades, the times at which the tip vortex interaction occurs are somewhat offset from the times where the peak loading due to the bound potential field interactions occurs (close to the times where the top and bottom blades pass over each other). This is because the tip vortices produced by the top rotor with raked blades has a much larger distance to travel to interact with the bottom rotor compared with those produced by the straight-bladed rotor. Thus, we see that there are two important effects of rake: firstly, the bound potential field interactions are reduced due to the increased axial separation between the top and bottom rotors—particularly at the outer portions of the blade—and secondly, this increased separation changes the relative time at which the impulsive loading due to the bound potential field interactions and tip vortex interactions occur. For the particular cases considered here, the peak in the unsteady loading on the lower rotor blades of the straight-blade rotor system due to both bound potential field interactions and tip vortex interactions coincide, which produces a significant impulsive force. However, for the rotor system with raked blades, the difference in the times between when the peak loading due to bound potential field interactions and tip vortex interactions results in a total peak loading which is somewhat lower than the straight-bladed case. At radii inboard of approximately 75% of the blade tip radius, the unsteady loading calculated from the CFD simulations is also somewhat different to that calculated from the semi-analytical model. This might be due to the effect of the tip vortex and other flow features (such as viscous wakes from the top rotor) which are captured in the CFD simulations but are not included in the semi-analytical model.

Figures 8 and 9 present contour plots showing the magnitude of the Fourier harmonic of the axial force per unit span, $\widehat{\boldsymbol{F}}_x^{(n)}(r)$ (where n corresponds to the Fourier harmonic number), plotted against dimensionless radius (vertical axis) and harmonic number (horizontal axis) for the reference blades of

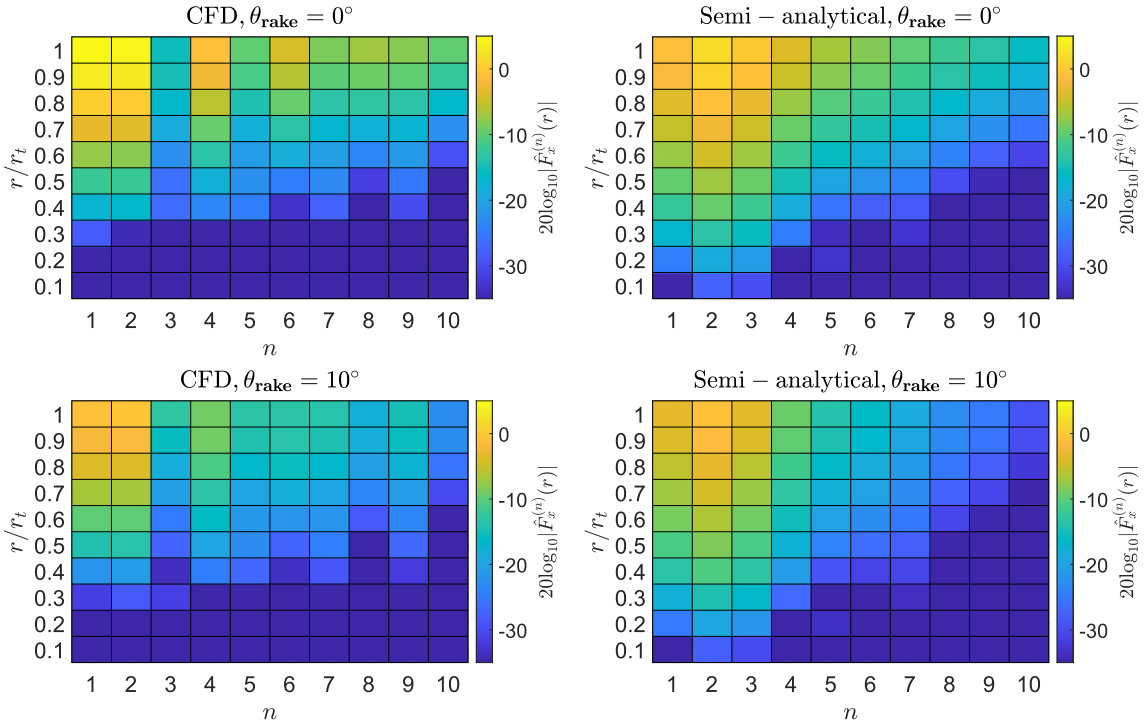

Fig. 8 Contour plots of the $20\log_{10}|\widehat{\boldsymbol{F}}_{\boldsymbol{x}}^{(\boldsymbol{n})}(\boldsymbol{r})|$ plotted against dimensionless radius (vertical axis) and harmonic number (horizontal axis) predicted using the loading data calculated from the CFD simulations (left-hand side) and semi-analytical model (right-hand side) for the top rotor reference blades. Results for the rotor system with straight blades are shown in the top subplots, whilst the results for the rotor system with raked blades are shown in the bottom subplots

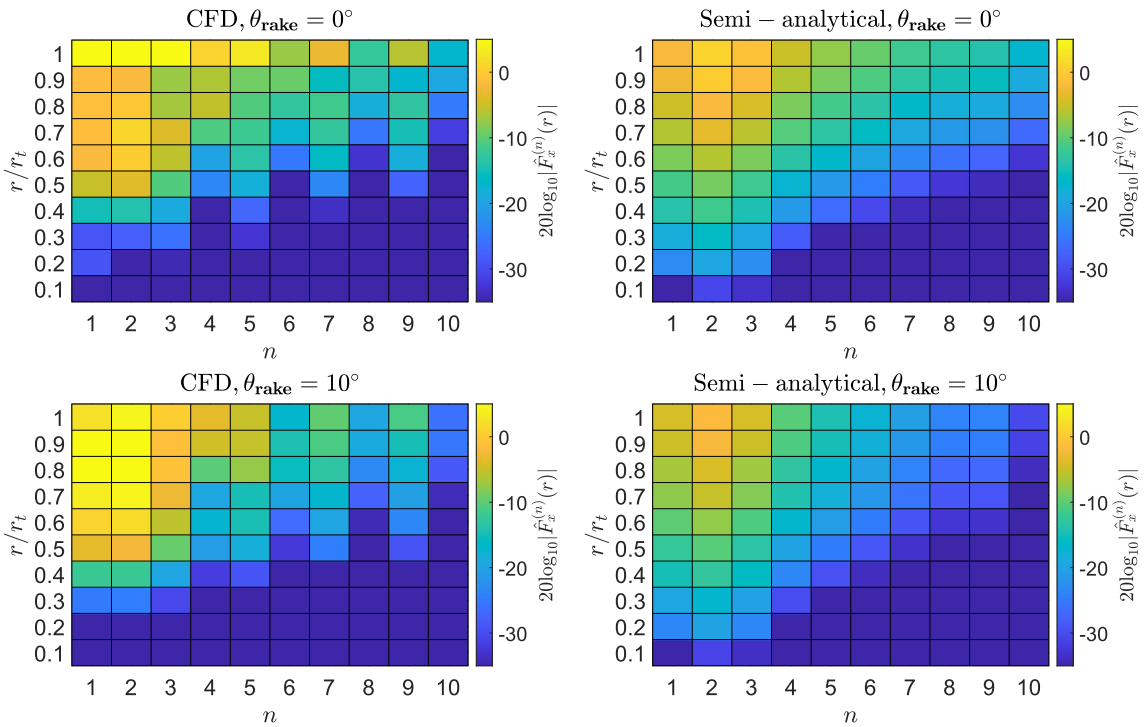

Fig. 9 Contour plots of the $20\log_{10}|\widehat{\boldsymbol{F}}_{\boldsymbol{x}}^{(\boldsymbol{n})}(\boldsymbol{r})|$ plotted against dimensionless radius (vertical axis) and harmonic number (horizontal axis) predicted using the loading data calculated from the CFD simulations (left-hand side) and semi-analytical model (right-hand side) for the bottom rotor reference blades. Results for the rotor system with straight blades are shown in the top subplots, whilst the results for the rotor system with raked blades are shown in the bottom subplots

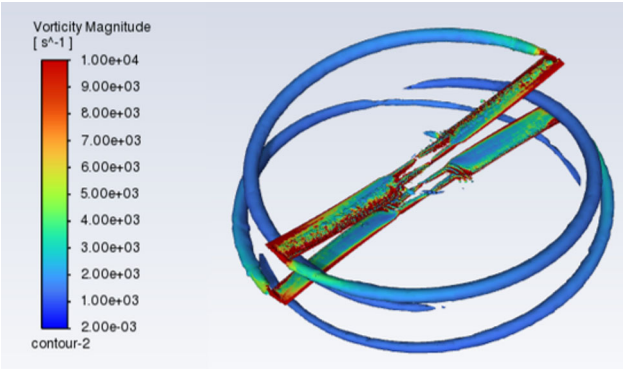

Fig. 10 Iso-surfaces of constant λ_2 criterion is plotted with the magnitude of the vorticity from the CFD simulation to estimate the trajectory of the tip vortex produced by the top and bottom rotor

the top and bottom rotors of the rotor systems with straight ($\theta_{\mathbf{rake}} = 0°$) and raked ($\theta_{\mathbf{rake}} = 10°$) blades. The results from both CFD and semi-analytical model show that most of the unsteady loading is produced by the first few harmonics and that the unsteady loading due to the bound potential field is strongest close to the tip/mid-span region for both top and bottom rotor blades for both the straight and raked rotor blade cases. Also, both results show that the magnitude of the unsteady loading near the tip for the top reference blade decreases as the blade rake angle increases. However, for the top reference blade, there are disparities for the third harmonic between the CFD and semi-analytical results. For the bottom reference blade in Fig. 7, the tip vortex impingement strongly affects the CFD results, which is not captured by the semi-analytical model.

Figure 10 presents a visualisation of the flow calculated from the contra-rotating rotor system with raked blades with a 40 mm gap. This plot displays iso-surfaces of constant λ_2 criterion coloured by vorticity magnitude, and it clearly shows the tip vortices shed from the rotor tips. These vortices convect downstream in a helical shape with a small pitch angle and travel radially inwards due to the stream tube contraction through the system. This plot was analysed to estimate the time and position of the tip vortex impingement for the analysis conducted in this study.

3.2 Radiated Interaction Tone Noise

In this section, the predicted sound pressure level of the prominent interaction tones produced by the rotor system with straight blades are validated against experimental measurements at various observer locations. Also, the predicted level of the radiated interaction tones for both rotor systems are compared at various observer locations. The influence of blade rake angle on the sound pressure levels of various interaction tones is explored across a broad range of rake angles using noise predictions made using loading data generated using the numerical and semi-analytical blade loading calculation methods. Finally, the overall sound pressure level of the straight and raked blades is compared to highlight the importance of lowering the level of these interaction tones.

The interaction tones occur at frequencies, $f = n_1\mathrm{BPF}_1 + n_2\mathrm{BPF}_2$, where BPF_1 and BPF_2 are, respectively, the blade passing frequencies of the top and bottom rotors and n_1 and n_2 are integers. In this paper, an interaction tone is specified by the value of n_1 and n_2. For example, the first interaction tone will be denoted as the $\{n_1 = 1, n_2 = 1\}$ interaction tone or the {1,1} interaction tone. The tonal spikes observed in the measured spectra are spread over a finite frequency band. A tonal sound pressure level was calculated for each tone using the method of McKay et al. [1]. This method involves integrating the power spectral density over the bandwidth of the tonal spike. The upper and lower frequencies which defined the bandwidth of the tonal spike were defined as the points which were 6 dB above the broadband noise level. The broadband noise level was calculated by fitting a moving median curve to the broadband spectrum.

In the cases analysed in this paper, the rotational speed of the top and bottom rotors was set to the same value, 500 rad/s, with both rotors having an identical number of blades. This setup results in multiple interaction tones occurring at the same frequency. To predict these tones, the contributions from each harmonic must be combined to calculate the total sound pressure level at a given frequency. For example, the second interaction tone occurs at frequency of 636 Hz which comprises contributions from the {1,3}, {2,2} and {3,1} interaction harmonics. So, the total sound pressure level for this tone was calculated by summing the contribution from all harmonics (although it may still be referred to here as the {2,2} interaction tone). It is important to note that the rotor systems considered here have an equal number of blades on the top and bottom rotors. As a result, the $n_1 = n_2$ interaction tones are the most prominent. These tones exhibit dipole-like directivity, with the highest levels near the axis of rotation and significantly lower levels near the plane of rotation [1].

Figure 11 presents the predicted and measured sound pressure levels for five prominent interactions tones produced by the rotor system with straight blades with all sound pressure levels normalised to a distance of 1.5 m, assuming spherical spreading. The reader should note that the noise predictions from CFD simulations and semi-analytical models were compared and validated at all polar angles from $\theta_{\mathbf{x}} = 0°$ to 150° in increments of 15°. For brevity, comparison between the measurements and predictions is presented at observer locations with polar angles, $\theta_{\mathbf{x}} = 0°$, 30° and 60°. Along with the acoustic measurements of the rotor system, the plot also displays the background noise levels at each observer location. The comparison between the predictions and the experimental measurements demonstrates good agreement. The comparison between numerical and measured sound

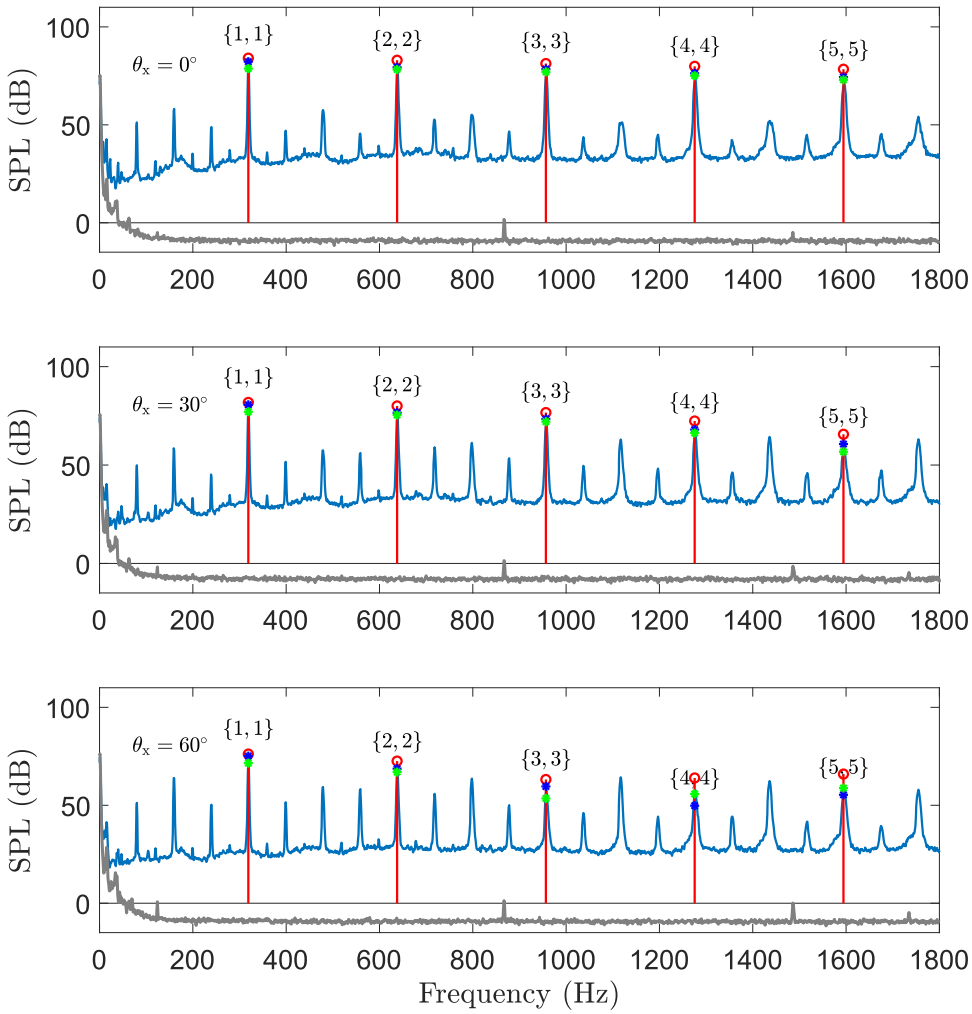

Fig. 11 Sound pressure level (SPL) spectrum produced by the rotor system with straight blades at an observer radius of 1.5 m at polar angles: $\boldsymbol{\theta}_{\mathbf{x}} = 0°$ (top), 30° (middle) and 60° (bottom). The blue curve is the narrow-band spectrum (1 Hz bandwidth), whilst the integrated tonal levels are shown by the red stems. The blue stars denote the predicted tonal levels from the CFD simulations. The green stars show the predictions from the semi-analytical model and the background noise levels are shown in grey

pressure levels for the {1,1}, {2,2} and {3,3} interaction tones is excellent across all observer locations, with a maximum discrepancy of only 2 dB. For higher frequency interaction tones such as the {4,4} and {5,5} interaction tones, the agreement between the predictions and measured sound pressure levels is good at polar angles near the axis of rotation (i.e. $\theta_{\mathbf{x}} = 0°$ and 30°) whereas the agreement is moderate at polar angles nearer the plane of rotation (i.e. $\theta_{\mathbf{x}} = 60°$). Overall, these results validate the numerical prediction tool and give confidence that it can be used to investigate the tonal noise produced by the contra-rotating UAV rotor systems considered in this paper.

The predicted sound pressure level for five different prominent interaction tones produced by the rotor systems with straight and raked blades is presented in Fig. 12. The results are presented for various observer polar angles but at the same azimuthal angle, $\phi_{\mathbf{x}} = 0°$. The tones produced by the rotor system with the raked blades have lower sound pressure levels at almost all observer locations. For the {1,1} and {2,2} interaction tones, the sound pressure level produced by the rotor system with the raked blades is lower than that produced by the rotor system with straight blades at all observer locations, except at polar angles very close to $\theta_{\mathbf{x}} = 90°$, where there is a null. The sound pressure level of the {3,3} interaction tone produced by the rotor system with the raked blades is lower than that produced by the rotor system with straight blades at polar angles near the rotor axis (i.e. $\theta_{\mathbf{x}} = 0°$). However, the polar angle corresponding to the minimum sound pressure level is slightly different for both cases. This shift results in a higher sound pressure level for the rotor system with raked blades than for the rotor system with straight blades at polar angles between $\theta_{\mathbf{x}} = 75°$ and 105°. As the polar angle increases further, the sound pressure level produced by the rotor system with straight blades surpasses that produced by the rotor system with the raked blades. Similarly, for the {4,4} interaction tone, the sound pressure level produced by the rotor system with straight blades is higher than that produced by the rotor system with straight blades near the rotor axis. However, near the rotor plane (between

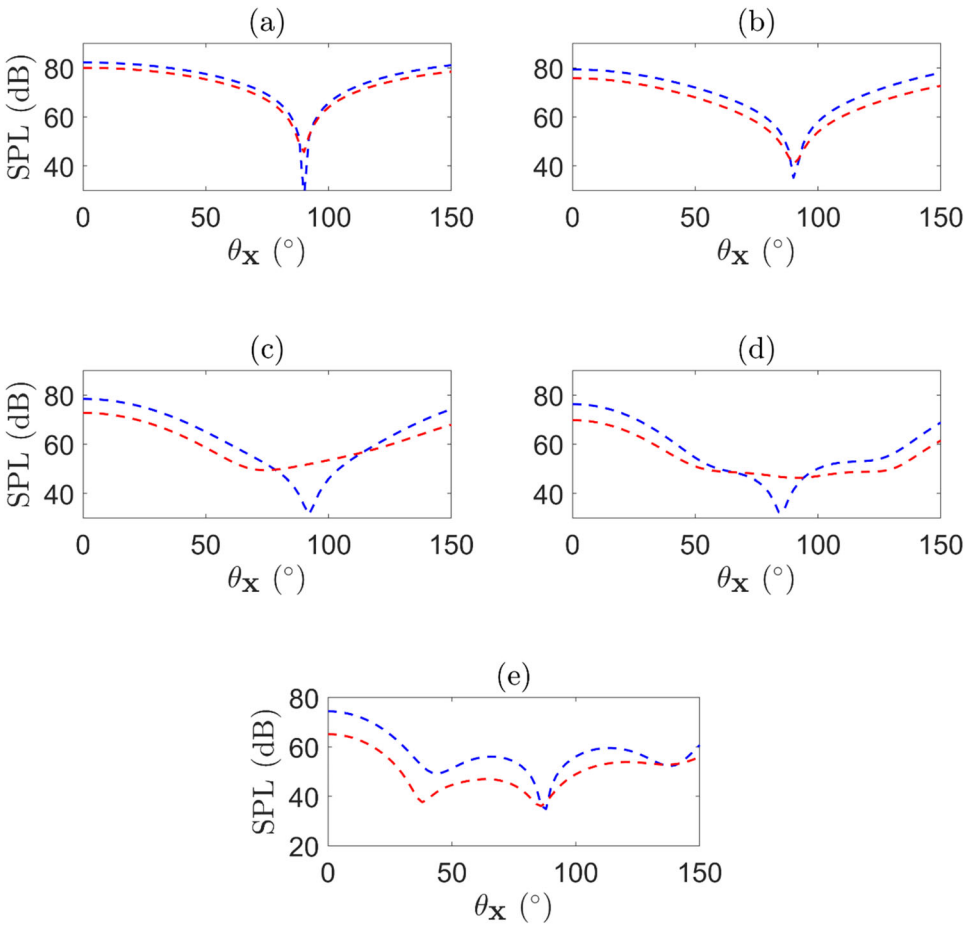

Fig. 12 Predicted sound pressure level polar directivity for five different interaction tones produced by the two different rotor systems operating at the same speeds. The rotor system with straight blades (i.e. $\boldsymbol{\theta}_{\mathbf{rake}} = 0°$) is shown in dashed blue curves, and the rotor system with rake blades (i.e. $\boldsymbol{\theta}_{\mathbf{rake}} = 10°$) is shown in red. **a** {1, 1} interaction tone, **b** {2, 2} interaction tone, **c** {3, 3} interaction tone, **d** {4, 4} interaction tone, **e** {5, 5} interaction tone

polar angles $\theta_{\mathbf{x}} = 75°$ and 95°), the levels are lower, comprising a local minimum at $\theta_{\mathbf{x}} = 90°$. Finally, for the {5,5} interaction tone, the sound pressure level produced by the rotor system with the raked blades is generally lower than that produced by the rotor system with the straight blades at all observer locations except very close to polar angles $\theta_{\mathbf{x}} = 90°$ and 135°, where the levels are similar.

The predicted sound pressure level from the loading data calculated using the semi-analytical model for five different prominent interaction tones produced by the rotor systems with straight and raked blades is presented in Fig. 13. The results are presented for various observer polar angles but at the same azimuthal angle, $\phi_{\mathbf{x}} = 0°$. Similar to the noise predictions based on CFD loading data, the tones produced by the rotor system with the raked blades have lower sound pressure levels at almost all observer locations. When compared to the noise predictions calculated from the loading data from CFD (Fig. 12), the directivity patterns of each tone are generally similar.

Figure 14 plots the numerical (CFD) and semi-analytical model predicted sound pressure level for five different interaction tones on the rotor axis at $\theta_{\mathbf{x}} = 0°$ produced by rotor systems with various blade rake angles. Numerical predictions were made for the two rotor systems with straight and raked blades considered previously ($\theta_{\mathbf{rake}} = 0°$ and 10°). The steady loading data and the velocity of the airflow induced by the rotors calculated from the CFD simulations for the straight-bladed rotor system were used as an input to the semi-analytical model for calculating the unsteady loading and consequent radiated tonal noise for rotor systems with different rake angles. The predictions from the semi-analytical model are calculated for blade rake angles ranging from 0° to 10°, in increments of 1°. The predictions made using the semi-analytical model are in modest agreement with the full numerical predictions in terms of sound pressure level. The reason for this is because the CFD accounts for the full flow field (taking account of potential field, viscous wake and tip vortex effects), and the analytical model only accounts for the bound potential field interactions. In addition, it is observed that the rate at which the sound pressure level decreases is observed to be larger for the higher frequency interaction tones. This is expected as the decrease is due to the reduction in the bound potential field interaction strength, and this model has been previously demonstrated to accurately capture this effect [7].

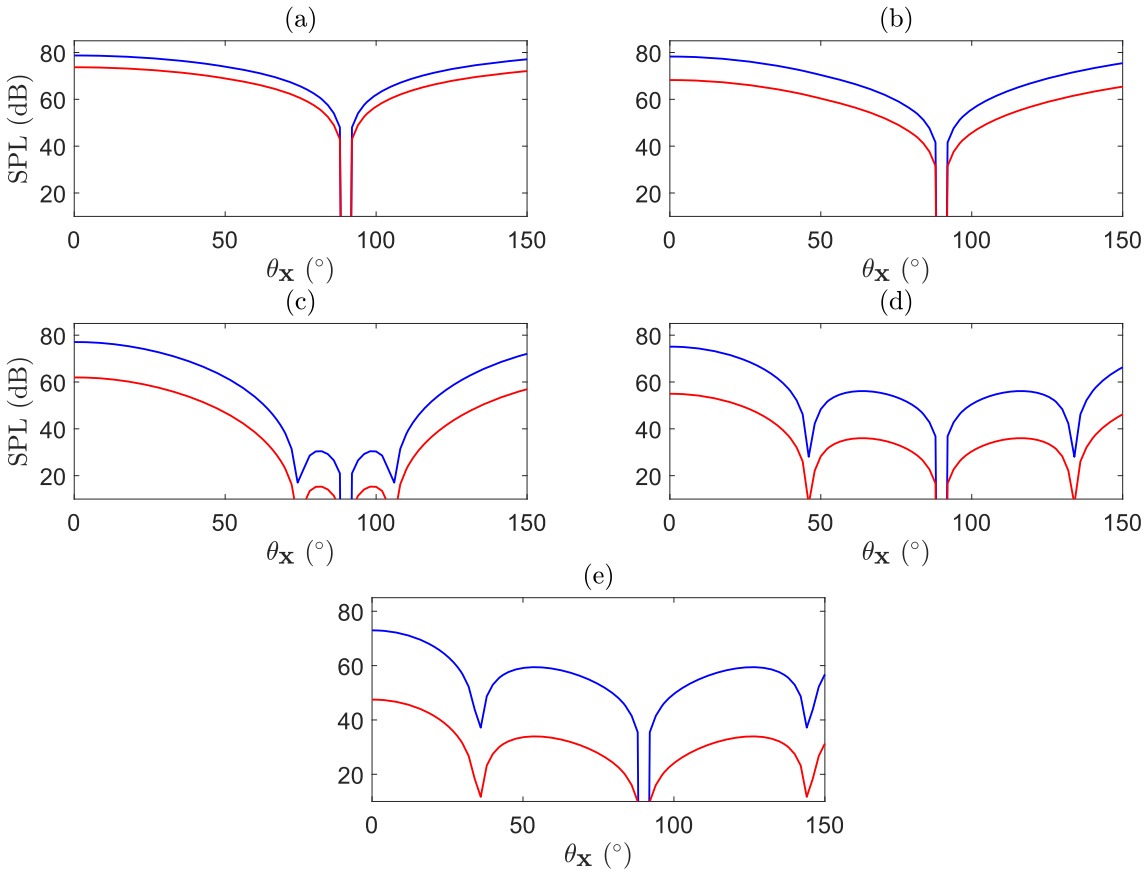

Fig. 13 Predicted sound pressure level polar directivity for five different interaction tones produced by the two different rotor systems operating at the same speeds. The predictions are calculated from the loading data calculated from the semi-analytical models. The rotor system with straight blades (i.e.$\boldsymbol{\theta}_{\mathbf{rake}} = 0°$) are shown in blue curves and the rotor system with rake blades (i.e.$\boldsymbol{\theta}_{\mathbf{rake}} = 10°$) are shown in red. **a** {1, 1} interaction tone, **b** {2, 2} interaction tone, **c** {3, 3} interaction tone, **d** {4, 4} interaction tone, and **e** {5, 5} interaction tone

Figure 15 plots the A-weighted overall sound pressure level which have been integrated over the frequency range from 20 Hz to 20 kHz against observer locations in polar angles from $\theta_{\mathbf{x}} = 0°$ to 150° in increments of 15°. The results show that the A-weighted overall sound pressure level produced by the rotor system with straight blades is higher than that produced by the rotor system with raked blades at all observer locations. The difference between the two signals is the greatest near the axis of rotation (i.e. 5 dB and 4 dB at polar angles, $\theta_{\mathbf{x}} = 0°$ and 150°, respectively) and this difference gradually decreases as the observer location gets closer to the plane of rotation (i.e. at polar angles, $\theta_{\mathbf{x}} = 90°$). At polar angle, $\theta_{\mathbf{x}} = 90°$, the difference is almost negligible with a difference of 0.4 dB. These results show that the decrease in the amplitude of the interaction tones produced by a contra-rotating UAV rotor system is crucial for reducing overall sound pressure levels, particularly along the axis of the rotation, where the noise levels are most significant.

3.3 Noise Reduction Analysis

The results presented in the previous section clearly show that rotor systems with larger rake angles produce lower levels of interaction tone noise. In this section, the reasons for this reduction are explored using noise predictions derived from the loading data obtained from the CFD simulations. To explore the reduction in noise, the loading data from the CFD simulations was extracted and analysed. The blades were divided into 10 radial segments, and the acoustic pressure variation with time was predicted for each segment at an observer location with a polar angle of 0° located a distance of 1.5 m from the centre of the top rotor blades.

The results for the sound radiated from the top rotor reference blades are presented in Fig. 16 (for the rotor system with straight blades) and Fig. 17 (for the rotor system with raked blades). In each figure, the top subplot shows the total acoustic pressure over one blade–blade interaction period. The bottom subplot displays contour plots of the acoustic pressure plotted against non-dimensional time (x-axis) and

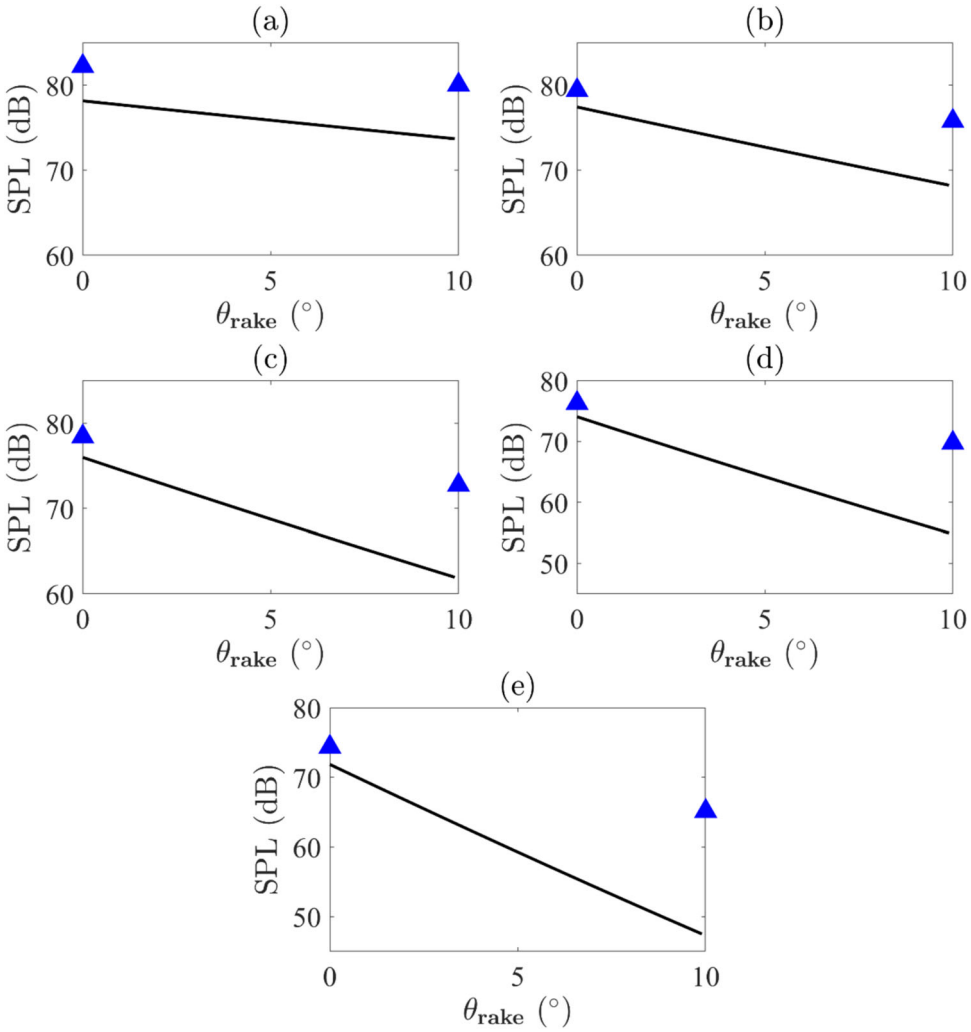

Fig. 14 Predicted sound pressure level versus $\boldsymbol{\theta}_{\mathbf{rake}}$ for five different interaction tones at $\boldsymbol{\theta}_{\mathbf{x}} = 0°$. Numerical predictions are denoted using blue triangles, whilst the semi-analytical predictions are shown using solid black lines. **a** {1, 1} interaction tone, **b** {2, 2} interaction tone, **c** {3, 3} interaction tone, **d** {4, 4} interaction tone, and **e** {5, 5} interaction tone

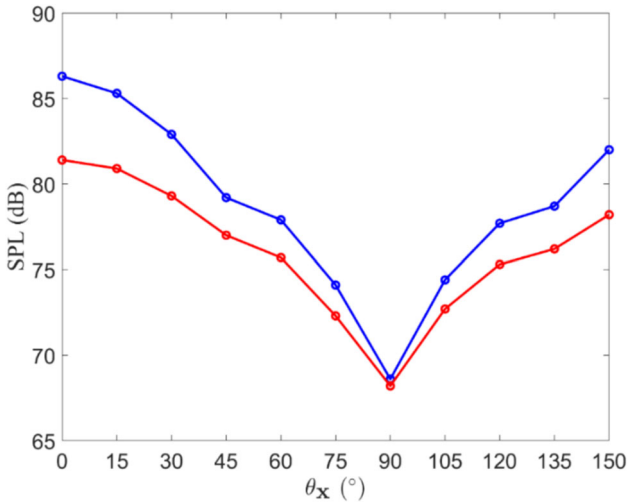

Fig. 15 Polar directivity plot for the A-weighted overall sound pressure level of the measured noise level produced by the rotor system with straight blades in blue and raked blades in red

non-dimensional radius (y-axis). The red dashed lines indicate the times at which the sound generated at the mid-chord of the top rotor reference blade when the mid-chords of the top and bottom rotor blades pass over each other reaches the observer's location. These plots reveal that the peaks in acoustic pressure produced by each radial segment align with the red dashed lines, indicating that the impulsive acoustic pressure results from bound potential field interactions. For the case with the raked blades, the magnitude of these acoustic peaks at each radius is lower than those produced by the rotor system with the straight blades. This suggests that the reduction in total acoustic pressure results from a weakened bound potential field interaction, caused by the increased axial distance between the rotors outwards along the blade span.

Similar results are produced for the bottom rotor and are shown in Figs. 18 and 19. As before, the red dashed lines in each lower subplot indicate the times at which the sound generated at the mid-chord of the bottom rotor reference blade when the mid-chords of the top and bottom

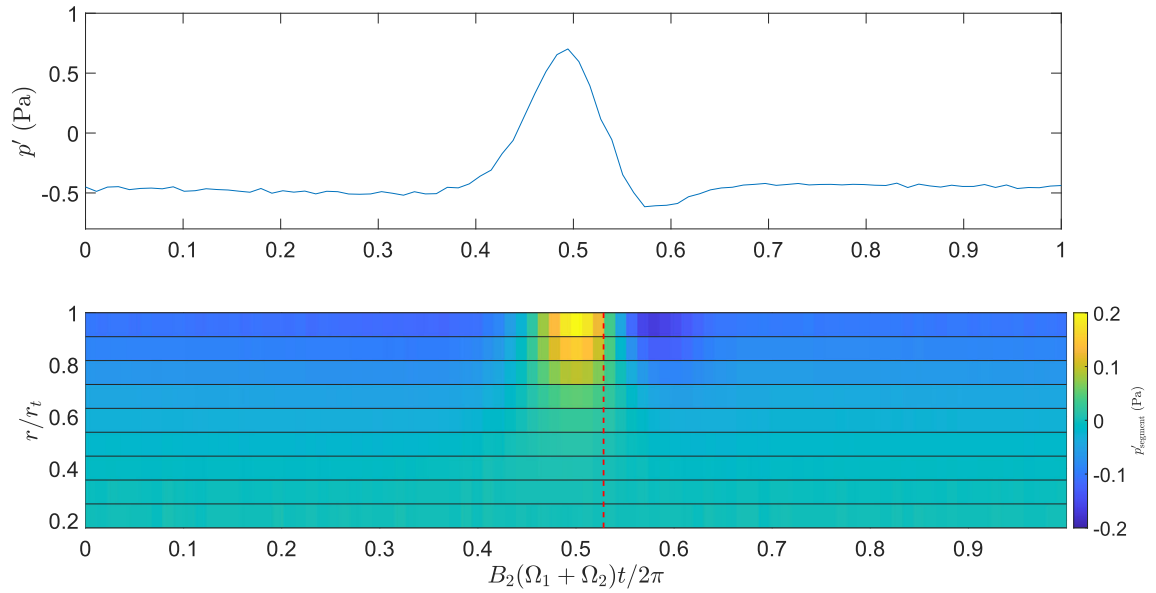

Fig. 16 The top subplot is the predicted total acoustic pressure time-history produced by the top rotor reference blade from the rotor system with straight blades. The bottom subplot is a contour plot of the predicted acoustic pressure radiated from each radial segment, plotted against the normalised radius (vertical axis) and normalised time (horizontal axis). The red dashed line shows the time at which the sound generated when the mid-chords of the top and bottom reference blades overlap reaches the observer location

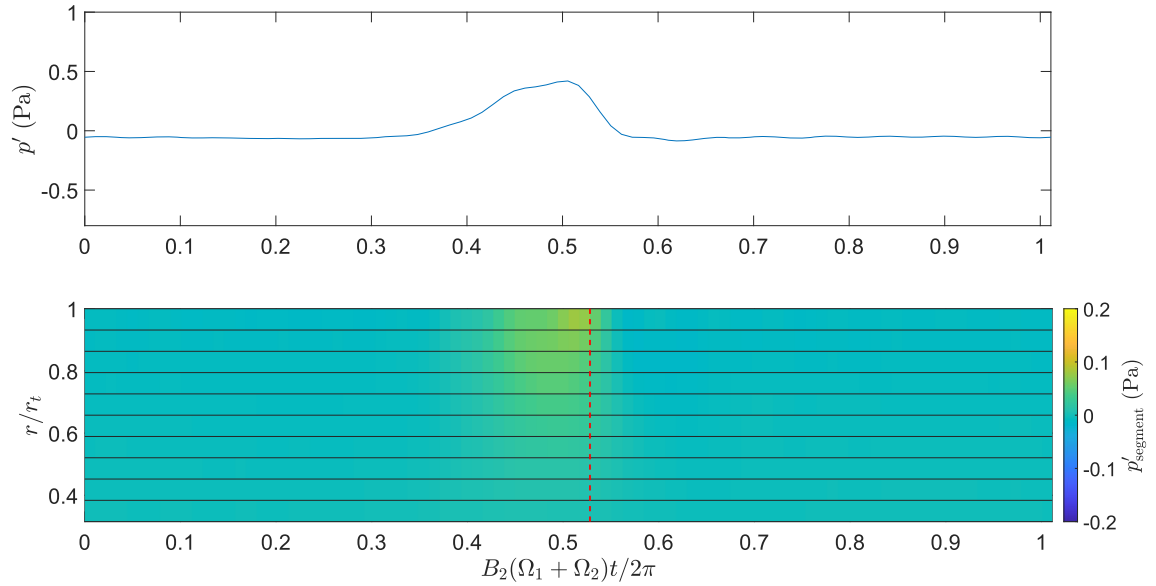

Fig. 17 The top subplot is the predicted total acoustic pressure time-history produced by the top rotor reference blade from the rotor system with raked blades. The bottom subplot is the contour plot of the predicted acoustic pressure radiated from each radial segment, plotted against the normalised radius (vertical axis) and normalised time (horizontal axis). The red dashed line shows the time at which the sound generated when the mid-chords of the top and bottom reference blades overlap reaches the observer location

rotor blades pass over each other reaches the observer position. In both lower subplots, there are peaks in the acoustic pressure which are likely associated with bound potential field interactions. However, in the outer segments, additional peaks in the acoustic pressure are observed which are caused by the tip vortex shed from the top rotor impinging on the outer portion of the bottom rotor. The approximate times at which the sound generated when a tip vortex interacts with the lower rotor reaches the observer is shown using red ovals. For the rotor system with straight blades, the tip vortex interaction occurs close to the time at which the blades overlap (which is when the bound potential field interaction is also strongest). This makes discerning what effects are due to

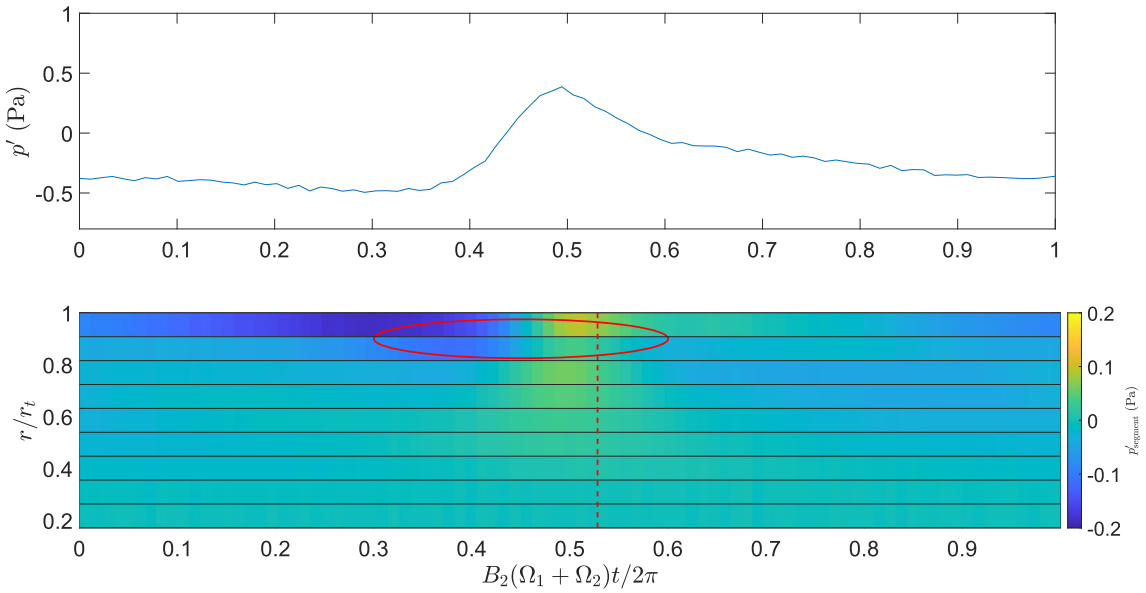

Fig. 18 The top subplot is the predicted total acoustic pressure time-history produced by the bottom rotor reference blade from the rotor system with straight blades. The bottom subplot is the contour plot of the predicted acoustic pressure radiated from each radial segment, plotted against the normalised radius (vertical axis) and normalised time (horizontal axis). The red dashed line shows the time at which the sound generated when the mid-chords of the top and bottom reference blades overlap reaches the observer location. The red solid oval shows the approximate times at which the sound generated when tip vortex interacts with the bottom blade reaches the observer

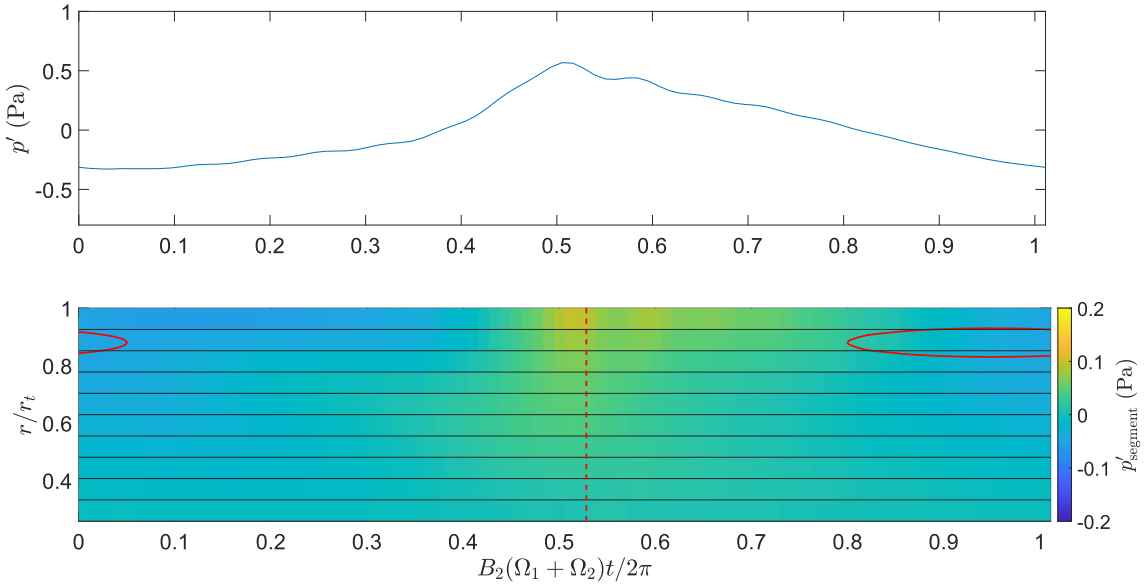

Fig. 19 The top subplot is the predicted total acoustic pressure time-history produced by the bottom rotor reference blade from the rotor system with raked blades. The bottom subplot is the contour plot of the predicted acoustic pressure radiated from each radial segment, plotted against the normalised radius (vertical axis) and normalised time (horizontal axis). The red dashed line shows the time at which the sound generated when the mid-chords of the top and bottom reference blades overlap reaches the observer location. The red solid oval shows the approximate times at which the sound generated when tip vortex interacts with the bottom blade reaches the observer

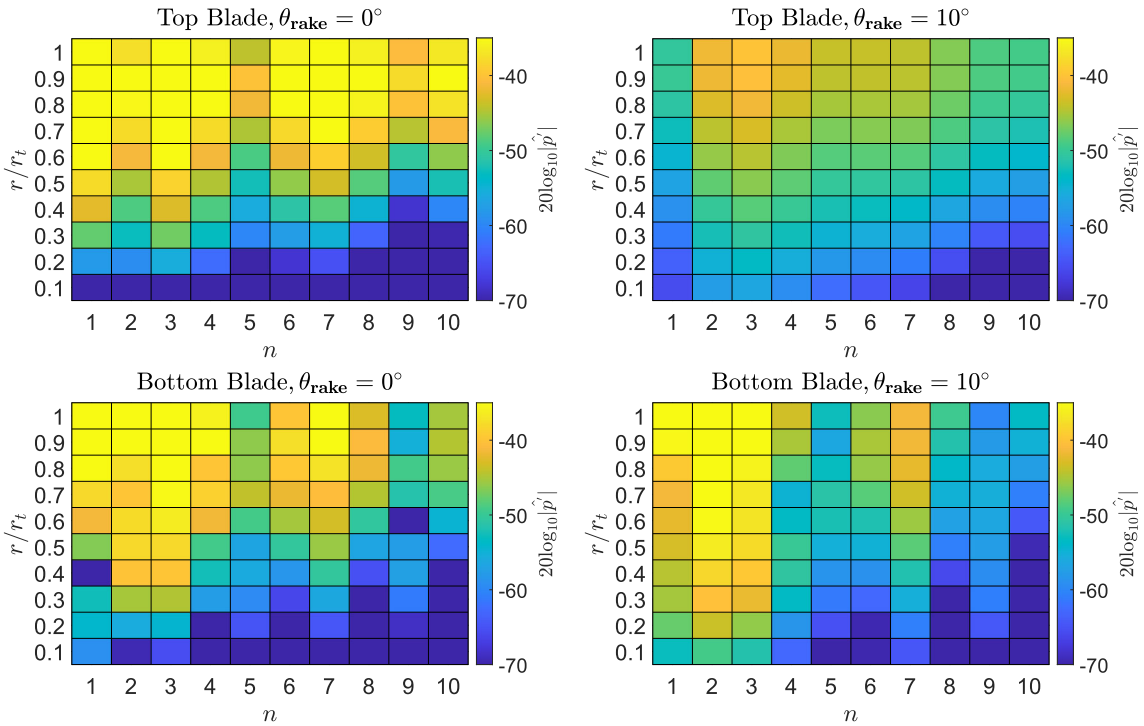

Fig. 20 Contour plots of the $20\log_{10}|\widehat{\boldsymbol{p}}|$ plotted against dimensionless radius (vertical axis) and harmonic number (horizontal axis) predicted using the loading data calculated from the CFD simulations for the top and bottom rotor reference blades. Results for the rotor system with straight blades are shown in the left-hand side subplots, whilst the results for the rotor system with raked blades are shown in the right-hand side subplots

what source of unsteady loading somewhat unclear. Nevertheless, the sharp discontinuity in the unsteady loading along the blade span, the difference in the nature of the plot in comparison to the top rotor plots (which only had contributions from the bound potential field sources) and the alignment of this strong unsteady loading with the tip vortex interaction time indicates that for this case, tip vortex interaction is a dominant source of unsteady loading on the outer portions of the lower rotor blades of the rotor system with straight blades. However, for the rotor system with the raked blades, although a bound potential field interaction is observed, there is no significant unsteady loading effect associated with the tip vortex interaction time (which for this case is offset from the blade-overlap time). This is somewhat unusual given we expect the bound potential field to decay as the axial blade separation distance increases, but for the tip vortex to persist downstream with its strength decaying only slowly.

Figure 20 presents contour plots showing the magnitude of the Fourier harmonics of the acoustic pressure $\widehat{\boldsymbol{p}}$ plotted against dimensionless radius (vertical axis) and harmonic number (horizontal axis) for the reference blades of the top and bottom rotors with straight ($\theta_{\mathbf{rake}} = 0°$) and raked ($\theta_{\mathbf{rake}} = 10°$) blades. The results show that for the top blade with $\theta_{\mathbf{rake}} = 0°$, the acoustic pressure produced is strongest close to the tip/mid-span region, whereas as the blade rake increases to $\theta_{\mathbf{rake}} = 10°$, the magnitude decreases significantly, especially for the first harmonic of the acoustic pressure. For the bottom blades, the acoustic pressure is the strongest near the tip/mid-span region. However, the magnitude of the acoustic pressure is significantly lower for the blade with 10° rake angle.

3.4 Tonal Loudness and Tonality

This section examines the impact of blade rake angle on the psychoacoustic properties of noise generated by contra-rotating UAS rotor blades. Figure 21 presents the sound pressure level spectrum of the synthesised noise signals produced by the two contra-rotating rotor system at $\theta_{\mathbf{x}} = 0°$ at a distance of 1.5 m from the centre of the top rotor. This location was selected because the levels of the interaction tones produced by these contra-rotating UAS rotor blades radiate most strongly along the axis of rotation of the rotors. Consequently, analysing the effect of the tip blade rake on the interaction tones at this location is particularly important. The sound pressure level spectra are dominated by interaction tones which occur at harmonics of the blade passing frequency, and the rotor system with straight blades produces interaction tones with significantly higher sound pressure levels. Both rotor systems have identical broadband noise spectra.

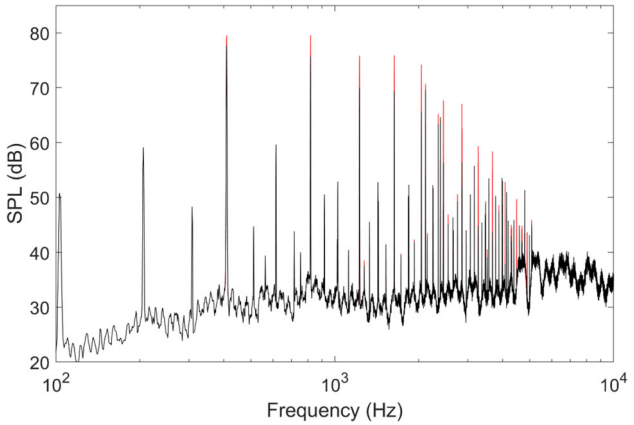

Fig. 21 Sound pressure level spectrum of the synthesised noise signal produced by the two contra-rotating rotor systems at $\boldsymbol{\theta_x} = 0°$ at a distance of 1.5 m. Rotor system with straight blades (red); rotor system with raked blades (black)

The Tonal Loudness and Tonality of the synthesised noise signals are shown in Fig. 22. On the left-hand side plot, a significant reduction of Tonal Loudness with the increase of the blade rake angle is observed. The Tonal Loudness of the rotor system with straight blades is higher by at least 0.2 soneHMS for all percentiles when compared with the rotor system with raked blades. The right-hand side plot presents the comparison of the Tonality calculated from the synthesised noise signals. Note that the noise perception metrics calculated using the original measured noise signal and the synthesised signal for the rotor system with straight blades were essentially identical (as shown in Figs. 23 and 24 in the appendix). It shows that the Tonality of the noise signal produced by the rotor system with straight blades is higher by at least 1 tuHMS for all percentiles when compared with the rotor system with raked blades. These reductions of both Tonal Loudness and Tonality suggest an expected reduction in noise annoyance with the increase of the blade tip rake angle from $\theta_{\mathbf{rake}} = 0°$ to $\theta_{\mathbf{rake}} = 10°$. This assumption relies on previous literature reporting tonal noise as one of the key factors driving annoyance for the noise produced by contra-rotating UAS rotors [18]. These results are consistent with Torija et al. [9], who found that as the axial distance between the top and bottom rotors increased, the perceived annoyance level of the noise produced decreased.

4 Conclusion and Future Work

This paper has investigated the effect of blade rake angle on the noise produced by contra-rotating UAS rotors in hover. With the use of semi-analytical, numerical and experimental methods, the aerodynamic loading, noise radiation and perceived noise signal have been thoroughly investigated.

Two sets of rotor systems were investigated using the numerical predictions, one with a blade tip rake angle $\theta_{\mathbf{rake}} = 0°$ (i.e. with straight blades) and another with $\theta_{\mathbf{rake}} = 10°$. CFD simulations and semi-analytical methods were used to predict the unsteady loading on the blades for each of the systems and the radiated noise was calculated using this data. Experimental data for the rotor system with straight blades were obtained from experiments conducted in the University of Auckland's anechoic chamber. Using this experimental data as the baseline case, a synthesis method was applied to separate out the broadband and tonal components of the noise signal. The reduction in the amplitude of the interaction tones produced by the rotor system with the raked

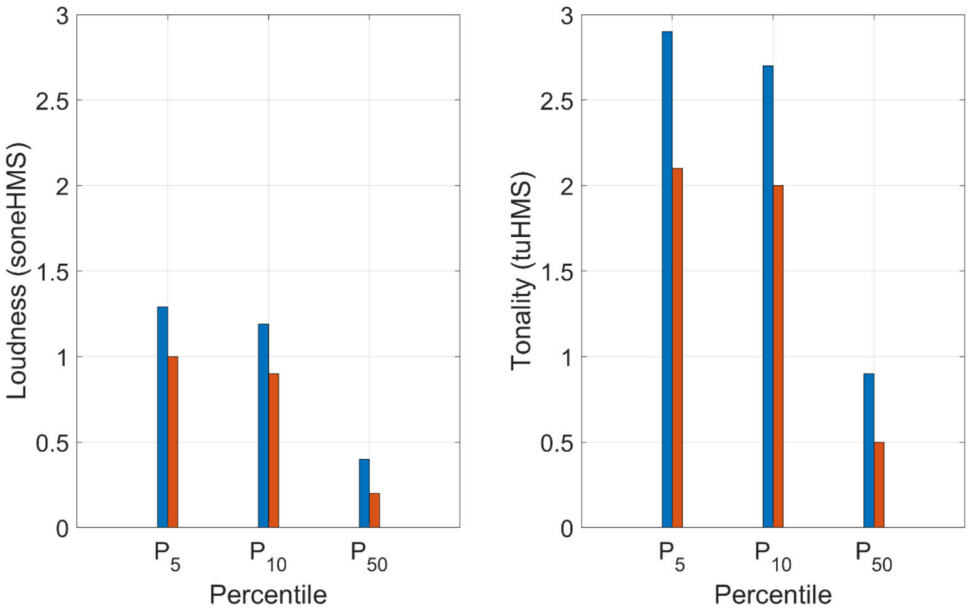

Fig. 22 Comparison of Tonal Loudness (left) and Tonality (right) for the rotor systems with blade tip rake angle $\boldsymbol{\theta_{\mathbf{rake}}} = 0°$ (denoted with blue bars) and 10° (denoted with orange bars) for the 5th, 10th and 50th percentile of the analysed data. The percentiles represent values below which the corresponding percentage of data points fall, with the 5th percentile indicating that 5% of the data are less than or equal to the corresponding Tonal Loudness or Tonality

blades was estimated from the numerical noise predictions. Through auralisation techniques, the estimated tonal noise and the broadband noise were combined and the noise signal produced by the rotor system with the raked blades was approximated. The Tonal Loudness and Tonality were calculated for both rotor systems, and a comparison was drawn.

The results indicate that increasing the blade rake angle generally reduces the amplitude of the prominent interaction tones at most observer locations. The unsteady loading analysis from both CFD and semi-analytical models indicates that the blade rake angle reduces the magnitude of potential field interactions, thereby decreasing the magnitude of acoustic impulses generated as the mid-chords of the top and bottom blades pass each other. With the semi-analytical methods, the noise radiation across a wide range of blade tip rake angles was investigated. The Tonal Loudness and Tonality of the noise signals produced by the rotor system with a blade tip rake angle $\theta_{\mathbf{rake}} = 10°$ were reduced (compared to that of the straight-bladed rotor), indicating that these blade geometry alterations positively impact the perception of the noise produced by contra-rotating UAS rotor systems.

This paper provides very useful insights into the physical mechanisms of noise generation by contra-rotating rotor systems, and the link with key psychoacoustic features. Therefore, the findings of this study are expected to aid the design of quieter and less annoying contra-rotating rotor configurations. It has been demonstrated that blade rake effectively reduces the amplitude of the interaction tones generated by contra-rotating UAS rotors, as well as their impact on tonal signal perception with a negligible compromise in the thrust production. Further work will focus on the study of the combined effect of blade rake and blade skew on the interaction tones produced by contra-rotating UAS rotor systems.

Appendix

Validation of the synthesis method

This section presents details of the validation procedure of the synthesis method presented in this paper. The noise signal for the blade rake angle of zero was synthesised and compared to the original measurement. Figures 23 and 24 present the spectrograms comparing the Tonal Loudness and the Tonality of the synthesised and original signals, respectively.

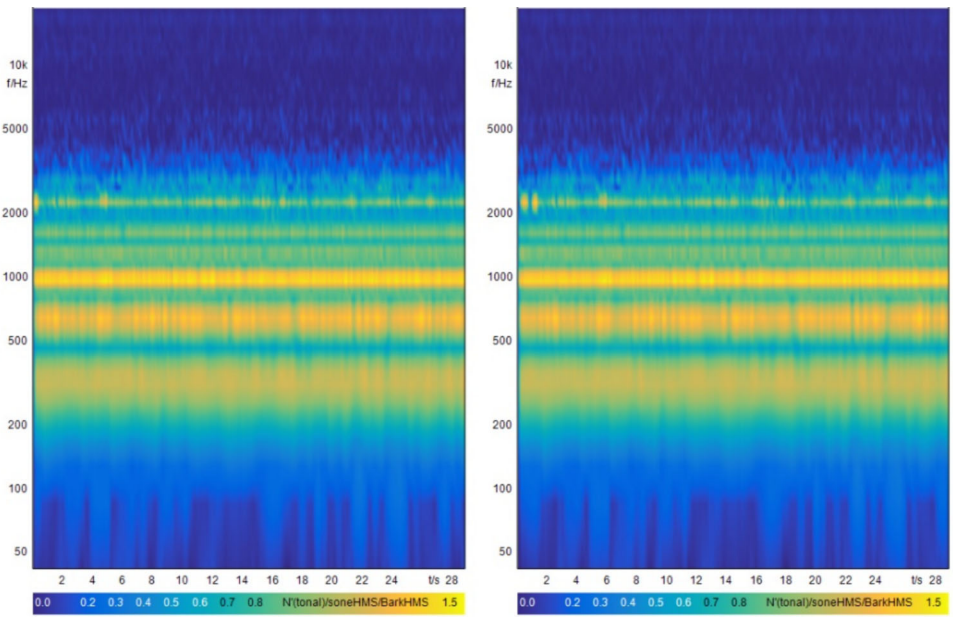

Fig. 23 Spectrogram of the Tonal Loudness calculated from the noise signal produced by the rotor system with straight blades. The original measurement taken in the University of Auckland's anechoic chamber is presented on the left and the synthesised signal is presented on the right. The *y*-axis shows the frequency (in Hz), the *x*-axis shows the time (in seconds), and the colour represents the magnitude of the Tonal Loudness (in Sones)

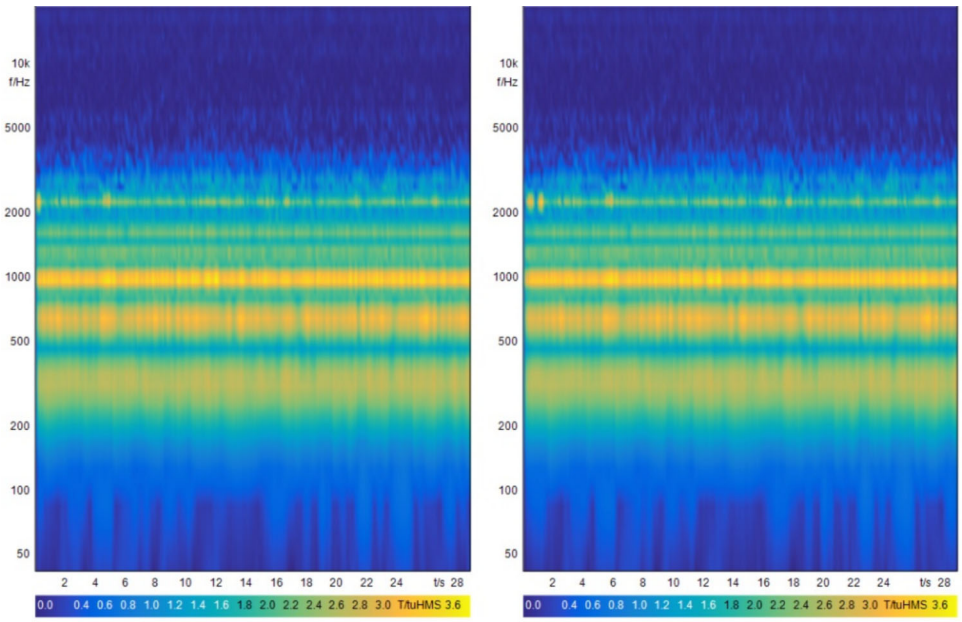

Fig. 24 Spectrogram of the Tonality calculated from the noise signal produced by the rotor system with straight blades. The original measurement taken in the University of Auckland's anechoic chamber is presented on the left and the synthesised signal is presented on the right. The *y*-axis shows the frequency (in Hz), *x*-axis shows the time (in seconds), and the colour represents the magnitude of the Tonality (in Tonality Units, TU)

Funding Funding was provided by Callaghan Innovation, Reducing Environmental Footprint through Transformative Multi-scale Aviation Planning (REFMAP), Impact and Capacity Assessment Framework for U-Space Societal Acceptance (ImAFUSA), Acoustics Research Centre at the University of Auckland, and Research Fellow at the University of Salford

References

1. McKay, R.S., Kingan, M.J., Go, S.T., Jung, R.: Experimental and analytical investigation of contra-rotating multi-rotor UAV propeller noise. Appl. Acoust. (2021). https://doi.org/10.1016/j.apacoust.2020.107850
2. Coleman, C.P.: A survey of theoretical and experimental coaxial rotor aerodynamic research. NASA Report, No. TP-3675, 1997, pp. 12–13
3. Hanson, D.B.: Noise of counter-rotation propellers. J. Aircr. **22**(7), 609–617 (1985). https://doi.org/10.2514/3.45173
4. McKay, R.S., Kingan, M.J., Go, R.: Experimental investigation of contra-rotating multi-rotor UAV propeller noise. Proc. Acoust. **1**, 1–10 (2019)
5. Chaitanya, P., Joseph, P., Prior, S.D., Parry, A.B.: On the optimum separation distance for minimum noise of contra-rotating rotors. J. Sound Vib. **535**, 110456 (2022). https://doi.org/10.1016/j.jsv.2022.117032
6. Zhong, S., Ma, Z., Zhou, P., Wu, H., Zhang, X.: Predicting the aerodynamic noise of counter-rotating coaxial rotors. J. Sound Vib. (2022). https://doi.org/10.1016/j.jsv.2022.117487
7. Jung, R., Kingan, M.J., Dhopade, P., Sharma, R., McKay, R.S.: Investigation of the interaction tones produced by contra-rotating unmanned aerial vehicle rotor systems. AIAA J. (2023). https://doi.org/10.2514/1.J062531
8. Jung, R., Kingan, M.J., Dhopade, P., Sharma, R.N., McKay, R.S., Dai, Z., Dymons, D., Pearse, J.: The effect of blade skew on the interaction tones produced by a contra-rotating UAV rotor system. J. Sound Vib. (2023). https://doi.org/10.1016/j.jsv.2023.118186
9. Torija Martinez, A.J., Chaitanya, P., Li, Z.: Psychoacoustic analysis of contra-rotating propeller noise for unmanned aerial vehicles. J. Acoust. Soc. Am. (2021). https://doi.org/10.1121/10.0003432
10. Casagrande Hirono, F., Robertson, J., Torija Martinez, A.J.: Acoustic and psychoacoustic characterisation of small-scale contra-rotating propellers. J. Sound Vib. (2024). https://doi.org/10.1016/j.jsv.2023.117971
11. ANSYS Fluent 12.0 Theory Guide (2009)
12. Farassat, F.: Derivation of formulations 1 and 1A of Farassat. Nasa/TM-2007–214853, Vol. 214853, No. March, 2007, pp. 1–25
13. Farassat, F., Succi, G.P.: A review of propeller discrete frequency noise prediction technology with emphasis on two current methods for time domain calculations. J. Sound Vib. (1980). https://doi.org/10.1016/0022-460X(80)90422-8
14. Ramos-Romero, C., Green, M.C., Torija, A.J.: Synthesis and auralisation of quadcopter flyovers for psychoacoustic assessment, in *30th AIAA/CEAS Aeroacoustics Conference* (2024). https://doi.org/10.2514/6.2024-3272
15. Akiwate, D.C., Joseph, P., Parry, A., Paruchuri, C.: On the balance between the tonal and broadband noise of isolated propellers. Int. J. Aeroacoust. **23**(1–2), 122–153 (2024). https://doi.org/10.1177/1475472X231225631
16. HEAD acoustics GmbH, ArtemiS Suite V16.2
17. Sottek, R.: A hearing model approach to time-varying loudness. Acta Acust. Acust. **102**(4), 725–744 (2016). https://doi.org/10.3813/AAA.918989
18. Torija, A.J., Li, Z., Chaitanya, P.: Psychoacoustic modelling of rotor noise. J. Acoust. Soc. Am. (2022). https://doi.org/10.1121/10.0009801